

ABSTRACT

BAKER, DAVID ANDREW. EXAFS Studies of Ge-Sb-Te Alloys for Phase-Change Applications. (Under the direction of Michael A. Paesler and Gerald Lucovsky.)

Studies of amorphous (a-) semiconductors have been driven by technological advances as well as fundamental theories. Observation of electrical switching, for example, fueled early interest in a-chalcogenides. More recently a-chalcogenide switching has been applied successfully to programmable memory devices as well as DVD technology where the quest for the discovery of better-suited materials continues. Thus, switching grants researchers today with an active arena of technological as well as fundamental study. Bond constraint theory (BCT) and rigidity theory provide a powerful framework for understanding the structure and properties of a-materials. Application of these theories to switching in a-chalcogenides holds the promise of finding the best composition suited for switching applications. Extended X-ray Absorption Fine Structure (EXAFS) spectroscopy is an ideally suited technique to investigate the switching properties of these materials. Films of amorphous $\text{Ge}_2\text{Sb}_2\text{Te}_4$, $\text{Ge}_2\text{Sb}_2\text{Te}_5$, and $\text{Ge}_2\text{Sb}_2\text{Te}_7$ exhibit differing bonding structures and bond statistics, which result in different electronic and optical properties. Results of new EXAFS experiments on these three critical compositions in the Ge-Sb-Te system are presented in light of BCT and rigidity theory.

EXAFS Studies of Ge-Sb-Te Alloys for Phase-Change Applications

By
David Andrew Baker

A dissertation submitted to the Graduate Faculty of
North Carolina State University
in partial fulfillment of the
requirements for the degree of
Doctor of Philosophy

Physics

Raleigh, North Carolina

2007

APPROVED BY:

Professor Gerald Iafrate

Professor David Aspnes

Professor Gerald Lucovsky
Co-Chair of Advisory Committee

Professor Michael A. Paesler
Co-Chair of Advisory Committee

DEDICATION

I dedicate this body of work to Dale Sayers. Dale's exuberance and curiosity spread to everyone around him, and with that excitement, he changed the world for the better. I am proud to have been his student, and I know that his memory will continue to inspire me in the future.

BIOGRAPHY

1979 saw the birth of one David A. Baker to a farm family in the rural Iowa town of Clear Lake. Through the following years, I took interest in the world around me, and delighted in the discovery of cause-and-effect relationships. Later in high school, this delight translated into scientific aptitude, which Blake Lobdell, my physics instructor, continued to nurture. As I applied to colleges and universities, however, my interest in physics took a back seat to music and theatre, and it was with these two vocations in mind that I wrote admissions essays and plotted my course of study for the next four years.

Eventually, I landed at Augustana College in Sioux Falls, SD, where, in addition to joining the choir, I took a chance on a chemistry course. Much to my surprise, I performed exceedingly well, prompting the professor of that class to encourage me to continue my scientific endeavors. With no real commitment to any one major, I felt the call of science again, and in four short years, I had completed a degree in physics with a minor in chemistry – all while singing in the choir and maintaining an active campus life involvement.

My junior year, I spent the summer at North Carolina State University working with Dr. Bob Nemanich on nano-patterning with an atomic force microscope. His enthusiasm brought me to seriously consider a career in physics, with the addition of grad school as a major component of my education. Nine months later, I received a call from Dr. Dale Sayers, who explained to me that he had an open position for a graduate student with a background in chemistry and physics. This position would require a lot of travel, and the willingness to work a few 24-hour shifts at large synchrotron radiation facilities. I agreed almost immediately, packed all my belongings into my car and drove 1200 miles from Clear Lake to Raleigh.

Here, I learned about x-ray absorption spectroscopy, solid state chemistry, and the joys of that 24-hour shift at the synchrotron. Those shifts, however, allowed me to engage Dale on a personal level, a feature of my graduate career I will always remember. Dale's untimely death in 2004, coupled with personal hardships and the impending departmental exams forced me to evaluate my commitment to the program. The program collaborators pressed me to continue, however, and I felt compelled to finish what I had begun.

Enter Michael Paesler. Michael agreed to serve as my advisor until I got back on my feet, offering help in the materials portion of my research. The absence of a leader in the EXAFS portion forced me to improve myself beyond my initial expectations, and Michael's intimate knowledge of the chalcogenide system forced me to better myself in that arena, as well. Now, three years later, I have Michael to thank for seeing me through to the end, even when I may not have believed in myself.

The future approaches, and quickly. I face whatever that future holds with determination and optimism.

ACKNOWLEDGEMENTS

Without the help of many influential people along the way, this dissertation could not have existed. Firstly, I thank Michael Paesler, for not only his advising over the years, but for his friendship and support when I needed them most. Gerald Lucovsky urged me to become what he called a “real spectroscopist”, one who looks beyond the first impression, digs deep into the guts of a technique, and figures out what is really underneath all those bumps, wiggles, and shoulders. I thank the rest of my advisory committee for their support and input: David Aspnes and Gerald Iafrate.

Secondly, I thank Art Edwards and Craig Taylor for giving me a glimpse into my future. Their patience and support pushed me to achieve better results, knowing that I too can contribute to real-world solutions.

Secondly, I thank Brian Rodriguez, Brian Davis, Eugene Bryan, Adam Hook, Grant Palmquist, and Joshua Smith for reminding me that breaks are an essential part of working and achieving.

Finally, I thank my parents for their undying belief in me.

TABLE OF CONTENTS

List of Tables	viii
List of Figures	ix
Chapter 1 Introduction	1
1.1 Introduction	1
1.2 Dissertation Organization	1
1.3 References	4
Chapter 2 Rigidity Theory	5
2.1 Introduction	5
2.2 Early Developments	6
2.3 Three Dimensional Networks	8
2.4 Conclusion	13
2.5 References	19
Chapter 3 The Intermediate Phase	20
3.1 Introduction	20
3.2 Experimental Identification of Rigidity Transitions	21
3.3 Raman Investigations of $\text{Ge}_x\text{X}_{1-x}$ glasses	21
3.4 Differential Scanning Calorimetry Experiments	22
3.5 TMDSC measurements in $\text{Ge}_x\text{X}_{1-x}$ glasses	27
3.6 Other glass systems	28
3.7 Conclusion	29
3.8 References	34
Chapter 4 Constraint Theory	35
4.1 Introduction	35
4.2 Introductory Constraint Theory	36
4.3 Broken Constraints	38
4.4 Expanding Constraint Theory	40
4.5 Conclusion	40
4.6 References	43
Chapter 5 Phase-Change Alloys and the Ge-Sb-Te System	44
5.1 Introduction	44
5.2 Phase Change Memory Technology	45
5.3 EXAFS Studies of Ge-Sb-Te alloys	48
5.4 Electronic Structure Calculations	50
5.5 Conclusion	52
5.6 References	56
Chapter 6 EXAFS Theory and Application	58
6.1 Introduction	58
6.2 A Short History of EXAFS	58
6.3 EXAFS Theory	60
6.4 Synchrotron Light Sources	65
6.4.1 Synchrotron Light	65
6.4.2 Beamline and Experimental Setup	66
6.5 Sample Preparation	68

6.6	Data Analysis.....	70
6.6.1	Background Removal.....	70
6.6.2	E to k Conversion and Weighting.....	71
6.6.3	Fourier Transform.....	71
6.6.4	Inverse Fourier Transform.....	72
6.6.5	Determination of Structural Parameters.....	73
6.7	References.....	81
Chapter 7	Results and Discussion.....	84
7.1	Introduction.....	84
7.2	EXAFS Results.....	84
7.3	Discussion.....	86
7.4	Constraint Counting.....	89
7.5	Conclusion.....	91
7.6	References.....	103

LIST OF TABLES

Table 3.1	Power laws for three regimes of CS mode in samples of $\text{Ge}_x\text{Se}_{1-x}$. For low x , a plot of $\log(v_{\text{CS}}^2(x) - v_{\text{CS}}^2(0.26))$ versus $\log(x - 0.26)$ is linear. For intermediate x values the slope has a power law dependence of 0.75 and at high x , the dependence is 1.54 33
Table 7.1	Coordination numbers (N), interatomic distances (R), phase shifts (E_0), and Debye-Waller factors (σ^2) for the $\text{Ge}_2\text{Sb}_2\text{Te}_x$ where $x=4, 5, 7$ 102

LIST OF FIGURES

RIGIDITY THEORY

Figure 2.1	14
Figure 2.2	15
Figure 2.3	16
Figure 2.4	17
Figure 2.5	18

THE INTERMEDIATE PHASE

Figure 3.1	30
Figure 3.2	31
Figure 3.3	32

CONSTRAINT THEORY

Figure 4.1	41
Figure 4.2	42
Figure 4.3	42

PHASE-CHANGE ALLOYS AND TE Ge-Sb-Te SYSTEM

Figure 5.1	54
Figure 5.2	55

EXAFS THEORY AND APPLICATION

Figure 6.1	75
Figure 6.2	76
Figure 6.3	77
Figure 6.4	78
Figure 6.5	79
Figure 6.6	80

RESULTS AND DISCUSSION

Figure 7.1	93
Figure 7.2	94
Figure 7.3	95
Figure 7.4	96
Figure 7.5	97
Figure 7.6	98
Figure 7.7	99

Figure 7.8	100
Figure 7.9	101
Figure 7.10	101

Chapter 1 - Introduction

1.1 Introduction

The work described in the following chapters represents the confluence of a theory and a technique well suited to investigate a problem of fundamental interest and technological import. The theory - constraint theory - provides a framework to understand amorphous material properties in terms of local bonding configurations. The technique, Extended X-ray Absorption Fine Structure (or EXAFS), provides just such information. The problem of interest, the structure of $\text{Ge}_x\text{Sb}_y\text{Te}_{1-x-y}$, is both a paradigm for constraint theory study as well as a key to development of a new generation of computing technology

To discuss the richness of the theory/technique confluence, one must first develop an understanding of three disparate but closely linked scientific arenas: constraint theory itself, rigidity theory, and the so-called intermediate phase. Then, to grasp the significance of experimental studies, one must develop a working knowledge of EXAFS and its application to Ge-Sb-Te alloys. With all of this firmly in hand, the structure and behavior of these alloys can be studied in detail. The chapters below follow this progression.

1.2 Dissertation Organization

The immediately following chapter begins the discussion through consideration of rigidity theory. This theory has deep historical roots in classical dynamics and has flourished most recently with the computational work principally in Michael Thorpe's group at Arizona State University. [Thorpe] While the foundations of the theory predate modern computational science, recent developments were made possible only through the use of computer calculations involving models of millions of atoms. The theory investigates deformations of

networks and distinguishes deformable from non-deformable regions. Thermodynamic considerations do not come into play in these studies that identify important rigidity transitions as rigidity percolates through the network. These transitions occur when $\langle r \rangle$, the average number of neighbors of atoms in the network, is approximately 2.4. This variable $\langle r \rangle$ – called the average coordination number – will find meaning as an important parameter throughout this dissertation.

Chapter three moves the discussion to the so-called “intermediate phase” of materials that are identified in terms of $\langle r \rangle$. Once again, the value $\langle r \rangle = 2.4$ specifies an important class of materials, whose coordination is bracketed by two values of $\langle r \rangle$, one slightly less than and one slightly greater than 2.4. Punit Boolchand and co-workers at the University of Cincinnati – the principal drivers of research on the intermediate phase – have used techniques ranging from Mössbauer spectroscopy, Raman spectroscopy and differential scanning calorimetry to identify the materials in this phase. [Boolchand, et al.] Their studies show remarkable quantitative consistency with the computational work on rigidity theory and encompass a range of binary and ternary chalcogenide glasses.

Chapter four presents the basics of constraint theory as formulated by Jim Phillips formerly of Bell Laboratories and currently at Rutgers University. Predating studies of the intermediate phase and numerical studies of rigidity, Phillips original work first identifies the special value $\langle r \rangle = 2.4$ from one very simple assumption. He submitted that when the number of constraints in a system exhausts the degrees of freedom in that system, a special kind of material results. This, he showed, is tantamount to identifying $\langle r \rangle = 2.4$ material. The initial work identified only one demarcating value of $\langle r \rangle$ and focused primarily on the

ease of glass formation. Subsequent study playing off both rigidity studies and intermediate phase investigations broadened the interpretation of constraint theory bringing it into close agreement with experiment and computation.

Chapter five presents a discussion of the materials of interest in this dissertation: amorphous ternary alloys of germanium, antimony, and tellurium. For certain compositions, some of these alloys have found technological application as memory storage devices. Currently used in optical recording media, devices of these alloys will soon be marketed as flash memory, and use of these materials in other memory applications is on the near horizon. Some device parameters are presented in this chapter, and technological considerations to future uses are discussed.

The three theories mentioned above all depend on identification of local bonding configurations so it is not surprising that x-ray spectroscopists employing EXAFS have joined the fray, concentrating their efforts in part on determining the average coordination value $\langle r \rangle$ for materials of interest to those studying rigidity, constraints, and the intermediate phase. The principal strength of EXAFS is to identify local bonding configurations, and a basic primer in EXAFS theory and experiment is presented in chapter six. EXAFS is a computationally intensive technique that exploits interference among primary and secondary photoelectrons involved with an x-ray absorption event to extract structural information. The chapter shows how the fine structure associated with this interference leads to information about local configurations near the atom associated with the primary photoelectron.

Chapter seven presents the main results of this dissertation: EXAFS studies of Ge-Sb-Te alloys. The data are interpreted in terms of constraint theory to determine the average

coordination for a number of alloy compositions. By surveying a range of compositions, a deeper understanding of a particular alloy's structure can be ascertained. Most notably, for compositions near a commercially popular alloy, $\text{Ge}_2\text{Sb}_2\text{Te}_5$, the material is in its intermediate phase. Trends as one varies the relative amount of Te in the sample reveals further information about sample properties and compositional trends. Study of the trends deepens ones understanding of Ge-Sb-Te alloys in particular and chalcogenide glasses in general.

1.3 References

Boolchand, P., Feng, X., and Bresser, W.J., *J. Non-Crystalline Solids* 293-295, 348 (2001).

Phillips, J.C., *Physics Today* **35**, 27 (1982).

Thorpe, M.F., *J. Non-Crystalline Solids*, **57**, 355 (1983).

Chapter 2 - Rigidity Theory

2.1 Introduction

Constraint theory and rigidity theory share a rich history that embraces systems as simple as sticks and balls and as complicated as quaternary phase change alloys. As later chapters will show, modern constraint theory is couched in terms of entropy and strain as a network undergoes a transition. Rigidity theory, on the other hand, considers the deformations of a network and address the problem in terms of the percolation of that network's non-deformable regions. In a sense this approach is simple, direct, and avoids thermodynamic complications. It addresses the deformability of a system at a fixed percolation transition.

As divergent as the two approaches may appear, they predict an identical transition threshold. Both suggest that the very nature of a network undergoes a transition as one changes the mean coordination of a material $\langle r \rangle$ through a value of 2.4. Defined more rigorously below, $\langle r \rangle$ may be considered simply to be the average number of nearest neighbors of atoms in a network. If the present volume has one theme, it centers on the nature of networks whose average mean coordination is approximately 2.4.

Early works in the development of constraint and rigidity theory lead in the present chapter to a discussion of the percolation of rigidity in three-dimensional networks of atoms. Following mean field numerical studies of systems of 2-, 3-, and 4-fold coordinated atoms, the discussion leads to the identification of an intermediate phase that is rigid but stress free.

The immediately following chapters deal in turn with an alternative approach to the transition that occurs near $\langle r \rangle = 2.4$, and an investigation of the distinct intermediate phase

identified near this coordination. Focus for now, however, on the nature of rigidity and its percolation through a network.

2.2 Early Developments

Lagrange considered the behavior of a system in terms of how that system is constrained [Lagrange]. The elegance and predictability of what is now referred to as *Lagrangian dynamics* underscore the power of his approach. Operationally, Lagrange used the constraints of a system to first determine the so-called Lagrangian of that system. He then defined equations of motion (involving this Lagrangian) whose solution led to a description of how the system behaves as a function of time. The notion of first determining constraints and then describing behavior through a formalism based on these constraints is the hallmark of Lagrangian dynamics. The same sequential analysis likewise provides the foundation for rigidity theory.

Clerk Maxwell advanced constraint analysis through consideration of simple mechanical frameworks of rigid bars and flexible joints [Clerk Maxwell]. Bars were constrained to fixed length, but attachment of bars at the joints enjoyed freedom of angular movement as shown in a two-dimensional space in figure 2.1. A framework of connected bars and joints can exist in a family of identically connected frameworks called deformations. [Servatius and Servatius] A framework that has only trivial deformations associated with translations and rotations of the complete framework is said to be rigid.

Consider first two-dimensional frameworks. In the simplest of cases, a two joint framework connected by one bar would be rigid. That is, while the framework would be free to translate or rotate in the plane determined by its three components, no relative motion of

any of its components would be allowed as seen in figure 2.2a. A 3-joint, 2-bar framework would be free to change its internal structure through a change of the bond angle created by the two bars. Since the relative position of two joints could change, the framework is not rigid as seen in figure 2.2b. The 3-joint, 3-bar framework of figure 2.2c, on the other hand, would be rigid. The bars would brook no internal alteration of joint-to-joint distances. The tetragonal framework of figure 2.2d with 4-bars and 4-joints would not be rigid. And so it goes.

Clerk Maxwell discovered a general criterion for determining whether a two-dimensional framework of b bars and j joints would be rigid. He showed that the transition from non-rigid, or floppy, to rigid occurred when $b = 2j - 3$. That is, for

$$b < 2j - 3 \tag{1}$$

the framework is floppy. On the other hand when

$$b \geq 2j - 3 \tag{2}$$

the framework is rigid. The negative term of -3 reflects the two rigid degrees of translational freedom and one degree of rotational freedom of the planar b -bar and j -joint framework.

Graph theorists [Edmunds; Laman] placed the results of Clerk Maxwell on a more formal footing in the 1960s and 1970s with the derivation of theorems with identical results couched in terms of vertices and end points. These results – such as Laman’s Theorem – apply only to two dimensional graph theory.

Generalization of the graph theory approach resulting in Laman’s theorem breaks down because of the so-called “banana graphs” shown in figure 2.3 where a 9-joint 15-bar

framework is depicted. According to equation (2), such a framework is rigid. As the figure illustrates, however, rotation of each of the three rigid “bananas” is allowed in three dimensions, and the rigidity criterion is no longer met.

2.3 Three Dimensional Networks

Extension of the above arguments to three dimensions has been studied by – among others – M.F. Thorpe and coworkers [Thorpe, Jacobs, Chubynsky and Rader]. Their analysis applies to the so-called Continuous Random Network or CRN. For random networks the term *continuous* suggests that i) there are no boundaries in the structure of interest that demark changes in structure, and ii) all bars are terminated with joints that connect to at least one other bar. Thorpe’s approach applies from the outset to CRNs with joints that connect to two three and four bars. Motivation for this choice comes from the application of the analysis to glasses such as $\text{Ge}_x\text{As}_y\text{Se}_{1-x-y}$ and $\text{Ge}_x\text{Sb}_y\text{Te}_{1-x-y}$ where rigidity theory is particularly relevant. Following this lead, joints become atoms and bars become bonds between atoms.

Let N be the total number of atoms in a system under consideration. If, then, there are n_r atoms with coordination r , one has

$$N = \sum_{r=2}^4 n_r \quad (3)$$

which leads to a straightforward definition of the mean coordination $\langle r \rangle$ as

$$\langle r \rangle = \frac{\sum_{r=2}^4 r n_r}{\sum_{r=2}^4 n_r} . \quad (4)$$

A physical system of N atoms in three dimensional space has a total of $3N$ modes of vibration. These modes are of two types, those that cost energy and those that do not. There are $N_{\text{constraint}}$ of the former, and there are N_{zero} of the latter. Thus,

$$3N = N_{\text{constraint}} + N_{\text{zero}} \quad (5)$$

Here the $N_{\text{constraint}}$ designation reflects the facts that bond bending and bond stretching forces represents constraints to the system. When small displacements from equilibrium occur, these constraints result in appreciable changes in the Keating potential [Keating]. The N_{zero} designation is chosen to indicate that other so-called floppy modes of vibration are of such low energy that their frequencies on an applicable scale of interest may be considered to be zero. These modes are sometimes referred to as zero-frequency modes.

Allowing for one constraint for each bond associated with the stretching of that bond along its length, there are $r/2$ stretching constraints for each of the two atoms sharing the bond. In D -dimensional space there are

$$(D-1) \cdot r - D \quad (6)$$

bending constraints per atom. In 3-dimensional space with n_r atoms having a coordination of r between 2 and 4, equation (5) thus becomes

$$3N = N_{\text{zero}} + \sum_{r=2}^4 \left[\frac{r}{2} + (2r-3) \right] n_r \quad (7)$$

Let f be the fraction of floppy – or zero-frequency – modes so that

$$f = \frac{N_{\text{zero}}}{3N} = \frac{\left[3N - \sum_{r=2}^4 n_r \left[\frac{r}{2} + (2r-3) \right] \right]}{3N} \quad (8)$$

Equation (4) allows one to reduce this to the simpler form

$$f = 2 - \frac{5}{6}\langle r \rangle. \quad (9)$$

As shown in figure 2.4, f monotonically decreases as $\langle r \rangle$ increases until $\langle r \rangle = 2.4$, above which $f = 0$. This result was first reported by Döhler and co-workers [Döhler, et al.] Clearly for two-fold coordinated atoms such as Se with $\langle r \rangle = 2$ and consequently $f = 1/3$, the system is floppy. For a tetrahedrally bonded material such as Ge, the system is much more constrained and this is reflected in a total absence of zero-frequency modes. For Ge, therefore, $f = 0$. Moving between these two extremes in ternary compounds such as $\text{Ge}_x\text{As}_y\text{Se}_{1-x-y}$ and $\text{Ge}_x\text{Sb}_y\text{Te}_{1-x-y}$ more and more 3- and 4-fold coordinate atoms are added to the network, the concentration of the 2-fold coordinated chalcogen falls, and f decreases until $\langle r \rangle = 2.4$.

Numerical studies of 2-, 3-, and 4-fold coordinated networks have been undertaken by the Thorpe group [Jacobs and Thorpe 1995 and 1996]. These investigations provide considerable progress over earlier works [Feng and Sen; Feng et al.; Day et al.; He and Thorpe; Hansen and Roux] especially in dealing with the notion of rigidity percolation. Using what they call a “pebble game” Jacobs and Thorpe develop a system that enabled them to numerically study networks as large as 10^6 atoms. This pebble game may be applied in two or three dimensions and the results are quite revealing. Most notably, numerical calculations show that with increasing average coordination in a network, pockets of once-floppy regions first become rigid. Next, these pockets grow in size and number. Then growing pockets merge, and finally above a so-called threshold, rigidity percolates through the network. One complexity of the pebble game centers on the notion of redundant bonds.

These are bonds that are added to the network that do not change the rigidity locally although they increase the average coordination.

The richness of this numerical analysis of rigidity percolation is beyond the scope of the present discussion. Particularly instructive for now, however, are calculations of the fraction of zero-frequency modes, f . The simple analysis resulting in equation (9) predicts an abrupt change in the slope of f as a function of $\langle r \rangle$ that is not reproduced in the numerical analysis. For the numerical work, f behaves as shown by the dotted line in figure 2.4, approaching the values of f at low and high values of $\langle r \rangle$, but diverging from the two straight portions of the curve of figure 2.4 near $\langle r \rangle = 2.4$. Most instructive is an examination of the second derivative of f as a function of $\langle r \rangle$ as shown in the inset of figure 2.4. The data shown are for an amorphous silicon (a-Si) network from which bonds were removed as $\langle r \rangle$ decreased. This bond dilution resulted in a curve yielding the second derivative data shown. Perhaps most noteworthy is the fact that the cusp of this curve is within 1% of $\langle r \rangle = 2.4$ as predicted by Maxwell in his much simpler analysis yielding the condition for rigidity given by equation (2).

Thorpe and co-workers have the advantage of being able to visualize the changing network as the average number of bonds $\langle r \rangle$ increases. The dramatic change in sample properties manifest in the narrow peak of the inset of figure 2.4 is clearly evident in the visualizations of figure 2.5 [Thorpe, et al. 2000]. The left side of the figure represents a typical section of the bond-diluted a-Si with $\langle r \rangle = 2.7$ in which rigidity does not percolate while the right, with $\langle r \rangle = 2.40$, displays a region in which it does.

To understand the percolative transition indicated in figure 2.5, one must delve a bit deeper into the nature of rigidity and redundancy. Consider adding bonds to a network as one increases $\langle r \rangle$. A bond placed between two atoms that are already mutually rigid is called redundant. Rigid structures that contain no redundant bonds are minimally rigid or isostatic. In the figure the wide black bonds are over constrained while the thin black lines are isostatic. On the left, the rigid regions are thus seen to be relatively sparse and separated. The increase in average coordination between networks on the left and right side of figure 2.5 is only 1.5% yet the entire region shown becomes rigid and overconstrained. In this and other models Thorpe and coworkers always find the rigidity transition to be second order.

The first bonds added by Thorpe and coworkers [Thorpe, et al., 2000] are to a floppy network. Eventually regions of the model become isostatic- i.e. rigid but not stressed. Any move that involves a bond being redundant and thereby creating an overcompensated stressed region is not allowed. Eventually the entire network becomes isostatic and a stress transition evident in figure 2.5 is reached. (In actuality, <1% of the floppy modes were left in the calculation when strain became inevitable. The bond-bending term causes constraints associated with a given bond to sometimes allow for the removal of floppy modes and simultaneously induce strain.)

Just below the threshold of the stress transition, the entire network is essentially isotatic. The important consequence is that rigidity percolates through the system without any accompanying stress. The results suggest the existence of two transitions: a second order transition at a smaller mean coordination, and another first order transition at a higher mean

coordination to a stressed rigid state. These transitions bracket an intermediate phase, the experimental existence of which provides the topic of a subsequent chapter.

2.4 Conclusion

Rigidity theory provides a rigorous approach to the study of network properties as a function of mean coordination, but the richness of rigidity theory is only suggested in the above analysis. More detailed study allows for identification of the nature of the transition between phases and speculates as to the order of these phases. The brief synopsis here is meant to underscore the identification of an intermediate phase that lies at the heart of the present volume.

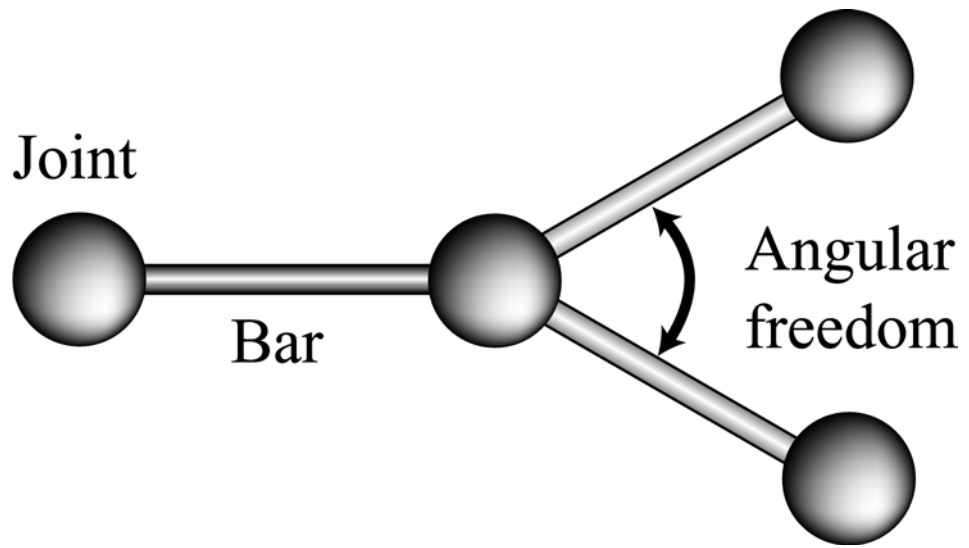


Figure 2.1 – Illustration of the Clerk Maxwell model for constraint analysis

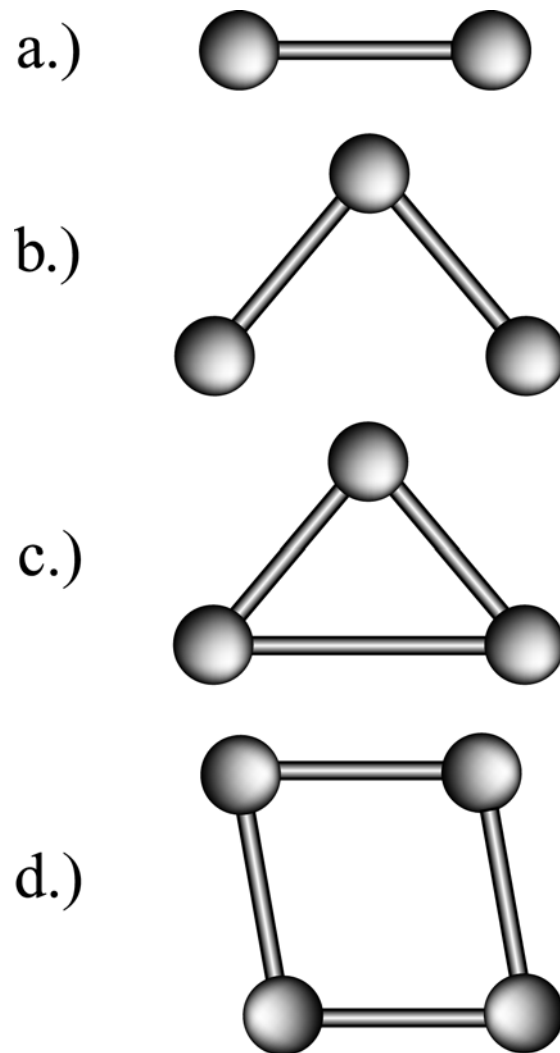


Figure 2.2 – Various two-dimensional frameworks with a.) 2 joints and 1 bar, b.) 3 joints and 2 bars, c.) 3 joints and three bars, and d.) 4 joints and 4 bars.

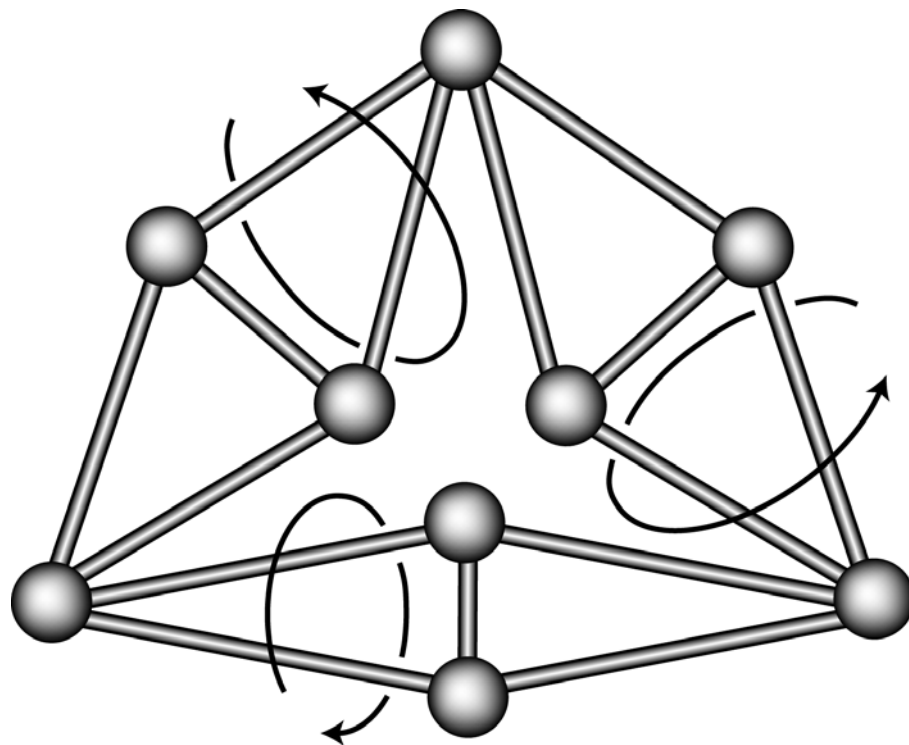


Figure 2.3 – A 9-joint, 15-bar framework illustrating the so-called “banana” rotations in three dimensions.

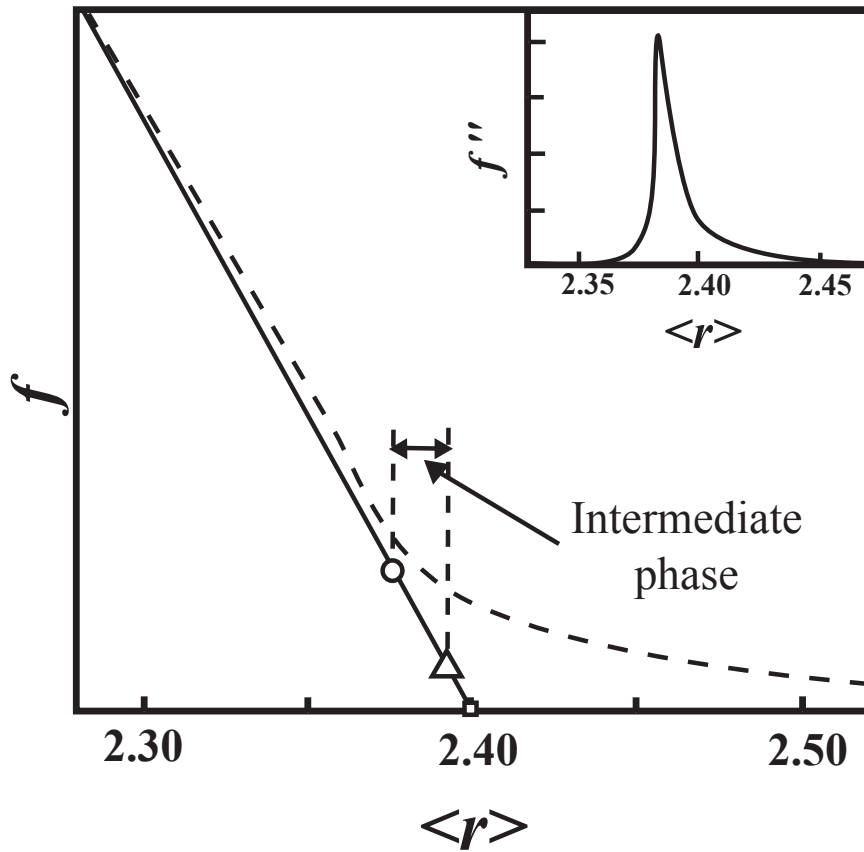


Figure 2.4 – Plot of average coordination $\langle r \rangle$ vs. fraction of floppy modes f . The solid line depicts the prediction of rigidity theory. The dashed line indicates the number of floppy modes found in the model. The intermediate phase is labeled between the open circle and open triangle. The inset shows the second derivative of the model, clearly illustrating the presence of a second-order phase transition.

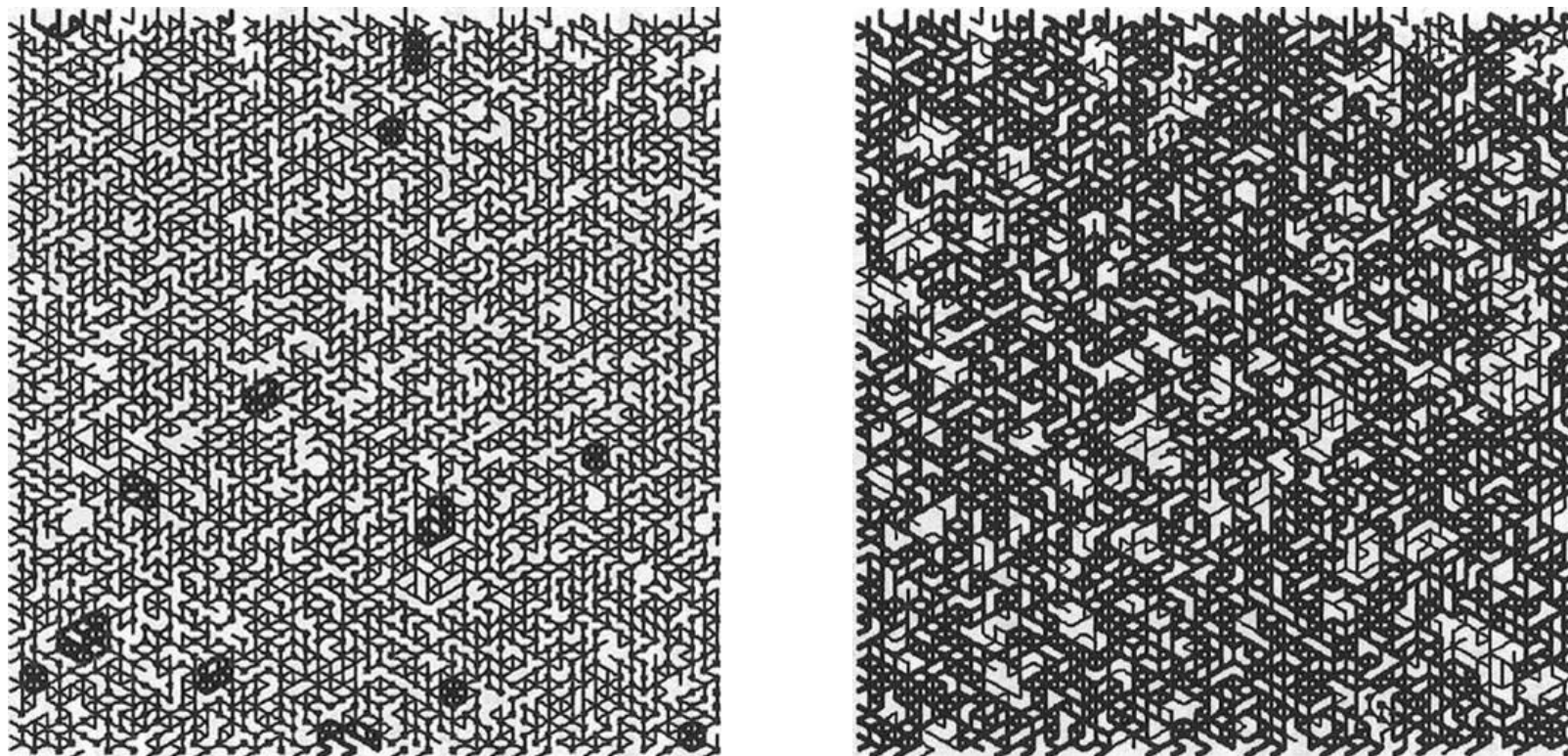


Figure 2.5 – Illustration of rigidity percolation as modeled in a-Si. The left side shows a bond-diluted structure, where the majority of bonds are isostatic. The right side shows a bond-saturated structure, where rigidity has percolated

2.5 References

- Clerk Maxwell, J., *Philos. Mag.* **27**, 294 (1864).
- Day, A.R., Tremblay, R.R. and Tremblay, A-M. *S. Phys. Rev. Lett.* **56**, 2501 (1986).
- Döhler, G.H. Dandoloff, R. and Bilz, H., *J. Non-Cryst. Solids* **42** (1980) 87.
- Edmonds, J., *J. Res. Nat. Bur. Standards B* **69**, 67 (1965).
- Feng, S. and Sen, P., *Phys Rev. Lett.* **52**, 216 (1984).
- Feng, S., Thorpe, M.F., Garboczi, E.J., *Phys Rev. B* **31**, 276 (1985).
- Hansen, A., and Roux, S. *Phys. Rev. B* **40**, 749 (1989).
- He, H. and Thorpe, M.F., *Phys. Rev. Lett.*, **54**, 2107 (1985).
- Jacobs, D., and Thorpe, M.F. *Phys. Rev. Lett.* **75**, 4051 (1995).
- Jacobs, D., and Thorpe, M.F. *Phys. Rev. E* **75**, 3682 (1996).
- Keating, P.N., *Phys. Rev.* **145**, 637 (1966).
- Lagrange, J.L., *Mechanique Analytique*, Paris (1788).
- Laman, G. *J. Engrg. Math.* **4**, 331 (1970).
- Servatius, B. and Servatius, H., in *Rigidity Theory and Applications*, Thorpe, M.F. and Duxbury, P.M., eds. Kluwer, NY, 1998, p. 1.
- Thorpe, M.F., Jacobs, D.J. Chubynsky, N.V. and Phillips, J.C., *J. Non-Crystalline Solids*, **266-269**, 859 (2000)..
- Thorpe, M.F., Jacobs, D.J. Chubynsky, N.V. and Rader, A.J., in *Rigidity Theory and Applications*, Thorpe, M.F. and Duxbury, P.M., eds. Kluwer, NY, 1998, p. 239.

Chapter 3 - The Intermediate Phase

3.1 Introduction

Impetus for studying – and experimentally identifying – an intermediate phase in glasses began with Phillips’ articulation of the simple notion that a transition should occur in a glass when the number of constraints exhausts the number of degrees of freedom, i.e. three in 3-dimensional space. [Phillips] Simple calculations showed that the Phillips criterion could be expressed in terms of the average coordination in a solid, usually given the symbol $\langle r \rangle$, and that the transition should occur at $\langle r \rangle = 2.4$. Shortly thereafter, Thorpe and colleagues provided a computational confirmation of such a transition. Thorpe’s numerical work characterized not one transition but two. [Thorpe] In doing so it suggested the existence of an intermediate phase between the two transitions. The investigation predicted transitions in network stiffness as the network’s connectivity increased. Experimental work reporting observation of just such a phase provided the final step in demonstrating the existence of the intermediate phase in glasses. [Selvanathan et al.]

The present chapter reviews first some of the initial work that established the intermediate phase before moving on to consider several systems that exhibit two transitions and an intermediate phase between them. The identification of myriad systems possessing an intermediate phase speaks to the universality of Phillips’ initial presumption. Later chapters will demonstrate further how the intermediate phase provides an arena for the application of constraint theory.

3.2 Experimental Identification of Rigidity Transitions

In one of the earliest attempts to identify the predicted transition, Boolchand's group investigated the stiffness of a covalently bonded network as a function of the mean coordination $\langle r \rangle$ in $\text{Ge}_x\text{X}_{1-x}$ glasses with $\text{X} = \text{S}$ or Se . [Feng et al.] Using Raman spectroscopy and differential scanning calorimetry (DSC) experiments, the group provided evidence for a stiffness threshold at a mean coordination given by $\langle r \rangle = 2.46$. This early result was encouraging in that it predicted a transition very close to the mean field value of 2.40 suggested for the onset of rigidity in random networks. Of course it was also very close to the numerical prediction of the Thorpe group. Presaging future work that would soon be undertaken by their own group and others, this Boolchand group study suggested that other IV-VI binary glass systems as well as IV-V-VI ternary systems such as Ge-As-Se alloys would also possess a stiffness threshold as mean coordination $\langle r \rangle$ in a series of glasses increase. A subsequent and more comprehensive study of bulk $\text{Ge}_x\text{Se}_{1-x}$ glasses also appealed to Raman and DSC results. [Boolchand et al., 2001]

3.3 Raman Investigations of $\text{Ge}_x\text{X}_{1-x}$ glasses

The Raman $\text{Ge}_x\text{X}_{1-x}$ results identified corner-sharing (CS) and edge-sharing (ES) $\text{Ge}(\text{Se}_{1/2})_4$ modes as well as Se_n chain modes (CM). [Boolchand et al., 2001] These well-characterized modes occur near 200 cm^{-1} and at 215 cm^{-1} for the CS and ES modes respectively and near 250 cm^{-1} for the CM mode. The data for these $\text{Ge}_x\text{Se}_{1-x}$ glasses appears as figure 3.1. Reading from bottom to top, each curve represents a successively larger $\langle r \rangle$ and presumably a stiffer network. As the network stiffens, the ES and CS modes grow at the

expense of the CM mode. The CS and ES modes could be fit with a single Gaussian making it possible to carefully track the peak position of these modes as a function of composition.

For the CS mode the authors constructed a plot involving a function of the frequency of the peak position ν_{CS} versus composition x for $\text{Ge}_x\text{Se}_{1-x}$. Two transitions occurred: one near $x \approx 0.20$ and the other near $x \approx 0.26$. These plots of $\log(\nu_{CS}^2(x) - \nu_{CS}^2(0.26))$ versus $\log(x - 0.26)$ thus revealed three distinct regions. In the low- x region, the curve was linear. In the intermediate and high- x regimes, the curves obeyed different power laws as indicated by the slope of the plots. The three distinct regions are described in terms of the power law behavior of the plots in Table 3.1.

Similar analysis of the ES mode revealed only two regimes: a linear regime for $x < 0.20$ and a 1.36 power law for $x > 0.20$. The CS data represent the first experimental evidence of a physical system exhibiting an intermediate phase. The difference between the first [Feng, et al.] Raman results and the second [Boolchand, et al., 2001] lies in the light intensity used to obtain the Raman data. In the latter work, the photon flux was more than three orders of magnitude less than in the former. The authors suggest that the early work was clouded by the possibility of light-induced modification of the rigidity transition.

3.4 Differential Scanning Calorimetry Experiments

Differential Scanning Calorimetry, or DSC, experiments echo the conclusions drawn from the Raman data. That is, the DSC data make it possible to identify three experimentally observed regimes as a function of composition with transitions between regimes occurring at essentially the same compositions as observed in the Raman study. While these results do indicate distinct observed behavior of a physical system in the intermediate composition

range, care must be taken in defining just what it is that one is measuring. One must consider these experiments in some detail to fully understand the observations. The outline below provides some detail about DSC work. It follows the discussion of Jiang and coworkers in their recent review. [Jiang, et al.]

In DSC studies, samples are heated or cooled at a constant rate while phase transitions are detected and properties such as temperature, heat capacity, and enthalpy changes are recorded. In TMDSC experiments, a periodic temperature modulation – usually sinusoidal – is superposed to introduce two differing time scales. A longer time scale corresponds to the monotonically varying temperature ramp and a shorter scale corresponds to the period of the periodic modulation. Typically the longer time scale may be many tens of minutes so that molecular relaxation times on this scale would come into play. The shorter time scale may be less than one minute, so interactions and motions of this much shorter duration would be involved.

In a DSC experiment, heat flow is comprised of two parts: the flow required to raise the temperature at a programmed rate; and the flow from kinetic processes that may occur as the temperature is varied. The latter may be melting, crystallization, glass transition, etc. For a sample of mass m and specific heat c_p heated at a rate β , one thus has a heat flow given by

$$\frac{dQ}{dt} = mc_p\beta + F(T,t) \quad (3.1)$$

where $F(T,t)$ represents the heat flow due to the kinetic processes.

In a TMDSC experiment, a modulation with frequency ω is added to the temperature ramp β so that if the temperature varies as $A_T \sin \omega t$ the heating rate q becomes

$$q = \frac{dT}{dt} = \beta + A_T \omega \cos \omega t. \quad (3.2)$$

A distinct advantage is involved with use of two widely varying rates; as the heating rate is increased, the sensitivity of the calorimeter increases, but as the rate is decreased, the resolution increases. Thus in TMDSC experiment, one rapidly varies the temperature as one slowly scans across a thermal transition while simultaneously measuring processes involving large and small heating or cooling rates.

In many of the investigations done to identify the intermediate state, the sample is not in thermal equilibrium in any of the transitions studied. In general, therefore, the enthalpy H is not a function of temperature T and pressure P alone. One must include an order parameter ξ so that

$$H = H(T, P, \xi) \quad (3.3)$$

and the change of enthalpy with temperature at constant pressure is given by

$$\frac{dH}{dT} = \left[\frac{\partial H}{\partial T} \right]_{\xi} + \left[\frac{\partial H}{\partial \xi} \right]_T \frac{d\xi}{dT}. \quad (3.4)$$

The left hand side of this equation is the apparent heat capacity while the first term on the right is the thermodynamic heat capacity. These two are zero only when the structural state of the sample – i.e. the order parameter ξ – remains constant. Multiplying equation (3.4) by a constant heating rate dT/dt , one obtains,

$$\frac{dH}{dt} = mc_{pb} \frac{dT}{dt} + \left[\frac{\partial H}{\partial \xi} \right]_T \frac{\partial \xi}{\partial t}. \quad (3.5)$$

Here the subscript b refers to the base-line specific heat capacity. In a DSC experiment the signal measured is just $P_{DSC} = dQ/dt$ so that

$$\frac{P_{DSC}}{\beta} = mc_{pb} + \left[\frac{\partial H}{\partial \xi} \right]_T \frac{\partial \xi}{\partial t}. \quad (3.6)$$

In a TMDSC experiment, one must add the modulation function (presumed to be sinusoidal) to the heating rate resulting in a measured signal P_{TMDC} given by

$$P_{TMDC} = P_{DSC} + \left\{ mc_{pb} + \left[\frac{\partial H}{\partial \xi} \right]_T \frac{\partial \xi}{\partial T} \right\} A_T \omega \cos \omega t. \quad (3.7)$$

It now becomes clear that there are two contributions to the TMDSC power: the DSC power and a modulated heat flow. The latter is complicated by the second term in the curly brackets which reflects contributions to the heat capacity from structural changes fast enough to occur during a modulation period. Often this term is neglected for simplicity. The term can be significant, however, when measuring melting and glass transitions, both of which can involve structural changes that may occur during one modulation period.

Neglect of these contributions to the heat capacity allows one to express the modulated component of the heat flow as

$$A_{HF} = mc_{pb,rev} A_T \omega \quad (3.8)$$

which leads to an expression for the apparent specific heat capacity

$$c_{pb,rev} = \frac{A_{HF}}{m A_T \omega}. \quad (3.9)$$

The designation $c_{pb,rev}$ identifies this as the reversing specific heat capacity. Note that it is different from the base-line specific heat capacity c_{pb} of equation (3.6). Namely, $c_{pb,rev}$ is frequency dependent.

The heat flow P_{TMDC} measured is often referred as the total heat flow HF_{tot} . If the second term in curly brackets of equation (3.7) is neglected and if no distinction is made

between $c_{pb,rev}$ and c_{pb} this is the same as P_{DSC} of equation (3.6). Typically one defines the product of $c_{pb,rev}$ and the heating rate as the reversing heat flow, or H_{rev} .

Difficulties occur when one makes what would appear to be a logical assumption that the total heat flow is the sum of reversible and non-reversible components. That is,

$$HF_{tot} = HF_{rev} + HF_{non-rev}. \quad (3.10)$$

In doing so, however, one assumes that there is no contribution to the modulated heat flow from structural changes that occur during one cycle and that the base-line heat capacity is identical to the frequency-dependent heat capacity. It is instructive to examine the applicability of these assumptions.

Only when one is in an equilibrium state – i.e. away from any structural transitions – is the first assumption valid. That is, outside a transition region, the modulated heating rate gives rise to a reversible modulated heat flow. Within a transition region, neither of the assumptions is valid. An alternative approach that avoids this problem is to introduce a complex heat capacity and then recognize that the contribution of structural changes would change the amplitude and the phase of heat flow modifications. The complex heat capacity would have two components: one in phase with the heating rate modifications and one out of phase. While several groups use this approach, there is no consensus on the meaning of the out of phase component. [Jeong; Schawe; Donth et al.; Höhne]

In the final analysis, TMDSC experiments must be interpreted with caution. Clearly the assumptions involved in using equation (3.10) to interpret results from most experiments are not well founded, and the response of materials to complicated thermal histories is not

well understood. Thus while TMDSC experiments may allow one to identify striking material behavior, just what this behavior indicates is moot.

3.5 TMDSC measurements in $\text{Ge}_x\text{X}_{1-x}$ glasses

Returning to rigidity transitions in germanium chalcogen systems, consider now DSC measurements as a function of composition. In the results referred to here, a TA Instruments calorimeter was used that generates two values for heat flow presuming the validity of equation (3.10). [Feng, et al.; Boolchand et al., 2001] The results are referred to as modulated DSC or MDSC data. Rather than trying to resolve the issues central to the interpretation of TMDSC measurements in general or the MDSC data discussed here, refer simply to the difference between the total heat flow and the reversible heat flow as ΔHF , or “delta HF.” Such a designation does not suggest one way or the other if the assumptions required for equation (3.10) to be valid are operational. This definition allows for either interpretation and supplants equation (3.10) with

$$HF_{tot} = HF_{rev} + \Delta HF. \quad (3.11)$$

The caveats of the previous section notwithstanding, the DSC measurements exhibit behavior remarkably similar to the previously quoted Raman results. They provide intriguing evidence for the existence of an intermediate phase. Plotted in figure 3.2 are the experimentally determined values of ΔHF as a function of Ge percentage in $\text{Ge}_x\text{Se}_{1-x}$ alloys. [Boolchand et al., 2001] Vertical lines are drawn to represent the demarcation compositions determined in the Raman experiments. As an alternative abscissa, the value of the mean coordination number $\langle r \rangle$ is indicated. Clearly ΔHF is a strong decreasing function of $\langle r \rangle$ in the floppy regime and is a strongly increasing function of $\langle r \rangle$ in the stressed rigid regime.

Within the error of the measurement, ΔHF vanishes in the intermediate phase between the two lines of demarcation.

3.6 Other glass systems

The Boolchand group has investigated a number of other glassy systems and finds evidence for the intermediate phase in all at very similar ranges of $\langle r \rangle$. The data for $\text{Ge}_x\text{As}_x\text{Se}_{1-2x}$ alloys shown in figure 3.3 exhibit a very similar $\Delta HF(\langle r \rangle)$ behavior. [Boolchand, et al., 2001] Perhaps most dramatic are the results from this group on $\text{Ge}_x\text{P}_x\text{Se}_{1-2x}$ alloys shown in figure 3.4. [Boolchand et al., 2005] Here the ΔHF curve “bottoms out” and becomes quite flat across the entire intermediate phase range. Because these researchers interpret the data to be reflective of the validity of equation (3.10), they term this region the “reversibility window.”

A characteristic of the intermediate phase becomes evident in aging studies where the MDSC experiments were performed on fresh, 3-month old, and 5-month old samples. Alloys in the intermediate phase show no signs of aging. This point is underscored in the discussion of Boolchand, Lucovsky, Phillips, and Thorpe [Boolchand, et al., 2005] where the intermediate phase is identified as a strain free range of compositions with a nearly constant density. They argue that as $\langle r \rangle$ increases in the intermediate phases, percolative strain-free backbones are added to the network and the phase is termed isostatic to indicate a lack of non-linear strain effects.

3.7 Conclusion

In a scenario involving theoretical, experimental, and computational advances, glass scientists succeeded in identifying a distinct intermediate phase in glasses. The agreement between the three approaches is remarkably quantitatively consistent: the intermediate phase spans a narrow range of coordination values $\langle r \rangle$ near $\langle r \rangle = 2.4$. The phase lies between a floppy phase that occurs at low $\langle r \rangle$ and a stressed rigid phase extending to higher values of $\langle r \rangle$. Subsequent chapters examine the behavior of alloys in the Ge-Sb-Te system in light of the arguments developed above.

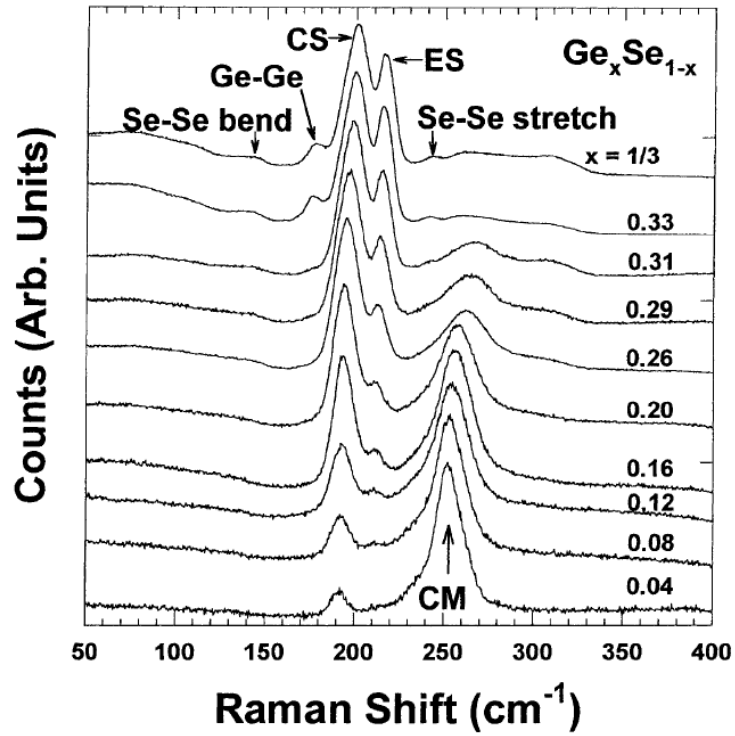


Figure 3.1 - Raman spectra of $\text{Ge}_x\text{Se}_{1-x}$ glasses taken in a macro-mode, showing growth in scattering of corner-sharing mode (200 cm^{-1}) and edge-sharing mode (215 cm^{-1}) scattering of $\text{Ge}(\text{Se}_{1/2})_4$ units at the expense of Se_n -chain-mode scattering (250 cm^{-1}).

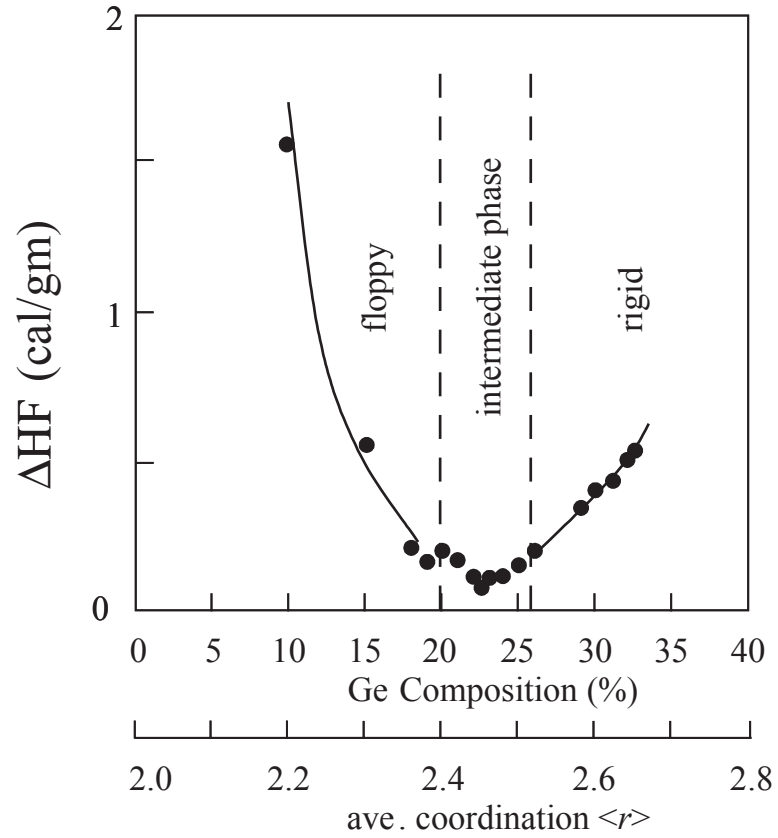


Figure 3.2 - Non-reversing heat-flow, $\Delta H_{nr}(x)$ variation in Ge_xSe_{1-x} glasses. The typical error associated with a datum is twice the size of the data point.

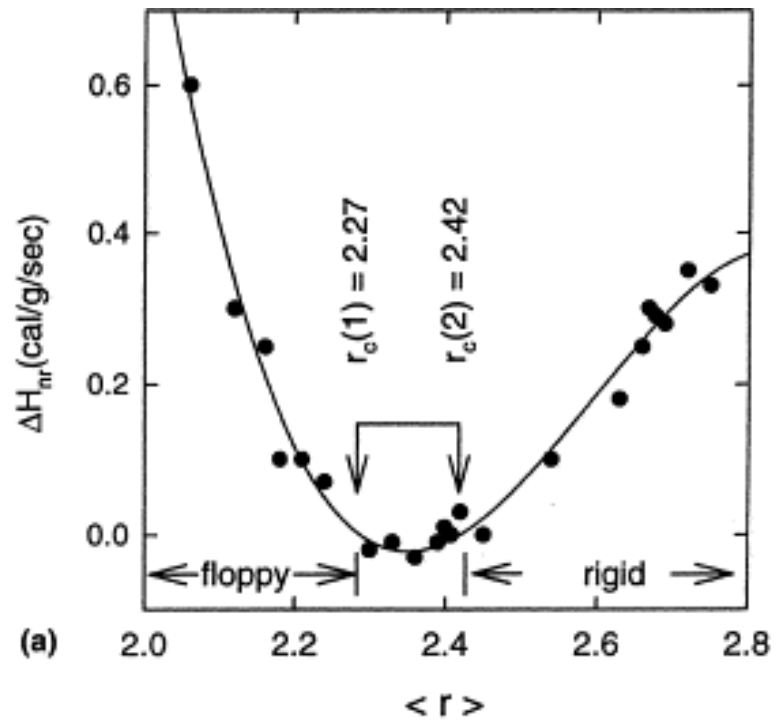


Figure 3.3 - Non-reversing heat-flow variation, ΔH_{nr} in $\text{Ge}_x\text{As}_x\text{Se}_{1-2x}$ glasses.

Tables

Table 3.1 Power laws for three regimes of CS mode in samples of $\text{Ge}_x\text{Se}_{1-x}$. For low x , a plot of $\log(v_{\text{CS}}^2(x) - v_{\text{CS}}^2(0.26))$ versus $\log(x - 0.26)$ is linear. For intermediate x values the slope has a power law dependence of 0.75 and at high x , the dependence is 1.54

$0.08 < x < 0.20$	$0.21 \leq x \leq 0.25$	$0.26 < x < 0.33$
linear	0.75	1.54

3.8 References

- Boolchand, P., Feng, X., and Bresser, W.J., *J. Non-Crystalline Solids* 293-295, 348 (2001).
- Boolchand, P., Lucovsky, G., Phillips, J.C., and Thorpe, M.F., *Phil. Mag.* **85**, 3823 (2005).
- Donth, E., Korus, J., Hempel, E., Beiner, M., *Thermochim. Acta* **304/305**, 239 (1997).
- Feng, Xingwei, Bresser, W.J., and Boolchand, P., *Phys. Rev. Lett.* **78**, 4422 (1997).
- Höhne, G.W.H., *Thermochim. Acta* **304/305**, 121 (1997).
- Jaing, Zhong, Imrie, Corrie T., Hutchinson, John M., *Thermochimica Acta* **387**, 75 (2002).
- Jeong, Y-H., *Thermochim. Acta* **304/305**, 67 (1997).
- Phillips, J.C., *J. Non-Crystalline Solids* **34**, 153 (1979).
- Schawe, J.E.K., *Thermochim. Acta* **304/305**, 11 (1997).
- Selvanathan, D., Bresser, W.J., Boolchand, P., and Goodman, B., *Solid State Commun.* **11**, 619 (1999).
- Thorpe, M.F., *J. Non-Crystalline Solids*, **57**, 355 (1983).

Chapter 4 - Constraint Theory

4.1 Introduction

Traditionally, seminal papers such as Zachariasen's have heralded advances in our understanding of glasses. In that 1932 paper, Zachariasen introduced the concept of the continuous random network. [Zachariasen] He argued that materials that form glasses would most likely have an internal energy somewhat larger in the amorphous state than in the crystalline state. It followed that the local atomic structure would be similar in the two phases. Perhaps most pertinent here is Zachariasen's suggestion that the non-periodic arrangement of atoms in a glass would result from a spread in bond angles and dihedral angles with very little variation in bond lengths. One now views this in terms of a minimization of strain energy or the tendency to form a floppy network.

In the next decade a kinetic aspect supplemented the structural view of glasses through an introduction of supercooling models based on kinetic rate theory. [Glasstone et al.] Then somewhat later, Kauzmann's important contribution added a more thermodynamic aspect to the consideration of glass formation in suggesting that the glass transition is best understood in terms of entropy and not enthalpy or volume. [Kauzmann] This idea echoes Zachariasen's notion that bond angle and dihedral angle – rather than bond length – distortions are more important in distinguishing the glassy from the crystalline state. In this view the excess (i.e. supercooled liquid as opposed to the crystal) thermodynamic quantities are described as *configurational*.

With a general theory relating structural differences to entropy changes lacking, Jim Phillips introduced in 1979 a fresh approach to the study of glass structure. [Phillips, 1979]

He considered atomic configurations in terms of the number of ways that atoms are constrained thereby casting unresolved issues in a new light by applying the long-established approaches of Lagrange and Clerk Maxwell. [Lagrange; Clerk Maxwell] Phillips' deceptively simple yet powerful and elegant relation identifies a class of materials possessing a structure that simply equates the number of constraints to the number of degrees of freedom.

4.2 Introductory Constraint Theory

Phillips' contribution equates the number of constraints in interatomic force field space, C_{av} , with the degrees of freedom in real space, D . That is

$$C_{av} = D. \quad (3.1)$$

In ordinary space, of course, $D=3$. Constraints may be bending constraints, call them f_b , or stretching constraints, call them f_s . In a compound described in terms of N atoms each with coordination r , a material with 2-, 3-, and 4-fold coordinated species would have average coordination $\langle r \rangle$ given by

$$\langle r \rangle = \frac{1}{N} \sum_{n=2}^4 r n_r \quad (3.2)$$

where there are n_r atoms of coordination r in each unit.

Each stretching constraint associated with any bond is shared by the two atoms it joins, so

$$f_s = r/2, \quad (3.3)$$

and in D -dimensional space, bending constraints for an r -fold coordinated atom are given by

$$f_b = (D-1) \cdot r - D \quad (3.4)$$

which in 3-space becomes

$$f_b = 2r - 3. \quad (3.5)$$

Now the total number of constraints, C_{av} , is simply the weighted sum of the stretching and bending constraints, or

$$C_{av} = \frac{1}{N} \sum n_r (f_s + f_b) \quad (3.6)$$

which reduces for 3-dimensional space and 2-, 3-, and 3-fold coordinated atoms to

$$C_{av} = \frac{1}{N} \sum_{n=2}^4 n_r \left(\frac{r}{2} + 2r - 3 \right). \quad (3.7)$$

In terms of the average coordination $\langle r \rangle$ given by equation 3.2, this reduces to

$$C_{av} = \frac{5}{2} \langle r \rangle - 3. \quad (3.8)$$

Phillips' condition (equation 3.1) identifies materials for which $C_{av} = 3$. The above expression allows one to characterize such materials in terms of average coordination $\langle r \rangle$.

That is, when the average coordination obeys

$$\langle r \rangle = 2.4 \quad (3.9)$$

the material satisfying this condition is identified by Phillips as having a number of constraints that precisely exhausts the number of degrees of freedom.

While current discussions of constraint theory center on the identification of an intermediate phase, the theory was initially cast in discussions of the glassforming ability of certain systems. Most notably, Phillips appealed to studies of the quenching rate of $\text{Ge}_x\text{Se}_{1-x}$ alloys. [Phillips] Appealing to data from Azoulay and co-workers, he plotted the glass forming ability of these alloys as a function of composition. An adaptation of these data

appears as figure 4.1. [Azoulay et al.] In the top of the figure (above the dashed line), the glassforming difficulty as one might presume from Phillips initial arguments based on constraint theory. The light gray area (where glasses easily form) represents a composition region for which glasses form when the melt is slowly cooled. Note that the value $\langle r \rangle = 2.4$ falls within this region. For larger and smaller $\langle r \rangle$ values, the melt must be more rapidly air quenched in order to form a glass. This is the slightly darker grey region. Finally for regions significantly removed from $\langle r \rangle = 2.4$ one must water quench the material to form a glass. These are the dark grey regions. To first order, the regions on the top of figure 3.1 support the arguments of Phillips suggesting that alloys with $\langle r \rangle = 2.4$ represent a distinct type of material. When constraints balance the degrees of freedom, a special sort of alloy results.

4.3 Broken Constraints

The data of Azoulay, however, do not follow upper regions depicted in figure 4.1, but behave instead like the regions shown below the dashed line. Over much of the $\langle r \rangle$ range, the two halves of the figure are quite similar. Near a compositions corresponding to roughly 40% Ge, however, a decided decrease in glassforming ability appears. (The authors did not discuss compositions for samples in the unshaded regions of the figure.) These data provide the exception that proves the rule and bring the discussion to the idea of broken constraints.

At the secondary minimum where air quenching can yield a glass, the material is $\text{Ge}_{0.4}\text{Se}_{0.6}$, or Ge_2Se_3 . At this composition, the material is comprised of the structural unit shown in figure 4.2, that is two Ge atoms bonded to each other with three other Se nearest neighbors. In alloys with no homopolar Ge-Ge bonds, Ge atoms would be bonded to four Se neighbors as shown in figure 4.2.

Consider the constraints on a Ge atom in the two alternative configurations of figure 4.2. When there are only heteropolar bonds (figure 4.2b), each Ge atom possesses stretching constraints related to its four neighbors. Each pair of bonds is constrained from bending, and the Ge atom might be considered to be maximally constrained. In figure 4.2a, however, the bending constraint involving two different neighbors (i.e. the one Ge neighbor relative to the three Se neighbors) would be relaxed as compared to that of figure 4.2b. One might view this as involving differing hybridization in the electronic bonding. Alternatively, one can argue that Pauli's exclusion principle for second neighbor Se-Se atoms is the cause of the bending constraints for the heteropolarly bonded configuration. Then in the homopolarly bonded case, second neighbor Se-Ge electronic wave functions overlap would relax this constraint somewhat. In terms of vibrational modes, the homopolarly bonded Ge of figure 4.2a would have much lower bending frequencies. Indeed, when these lower frequencies are modeled in chapter 2, they are called "zero-frequency" modes. However one views the situation, the argument is clear: the presence of homopolar bonds reduces the constraints in the system and allows an alloy to be more likely to form a glass. This – argued Phillips – is the origin of the air quenched region in figure 4.1 that occurs near $x = 0.4$.

The notion of constraint removal can be placed on a more quantitative footing when more complete information about local bonding statistics is available. In chapter 7, for example, calculations involving explicit constraint counting and removal based on EXAFS results allow one to determine the average number of constraints C_{av} to two significant figures.

4.4 Expanding Constraint Theory

After the initial framing of constraint theory simply in terms of glassforming ability, computational and experimental developments later showed the theory (and the identification of distinct materials near $\langle r \rangle = 2.4$) to have broader application. [Boolchand et al.; Phillips 1998] In addition, transitions as a function of $\langle r \rangle$ have been identified in a variety of experiments.

Constraint theory has been employed in explanations of the physical properties of window glass [Kerner and Phillips]; Si-SiO₂ interfaces [Lucovsky and Phillips]; and even proteins [Zavodsky et al.]. Techniques used to examine material properties in light of constraint theory have included Mössbauer, Raman, Differential Scanning Calorimetry, EXAFS, angular resolved photoemission, and others.

4.5 Conclusion

Born from the simplest of assumptions – a balance of constraints and freedom – bond constraint theory has grown to encompass a variety of materials and techniques. In the discussion that follows, the theory allows one to consider the properties of a family of chalcogenide glasses based on how the atoms of those glasses are constrained. The theory provides an insightful means of studying these space filling continuous random networks. In doing so it promises to allow for advanced development of these alloys of considerable technological value.

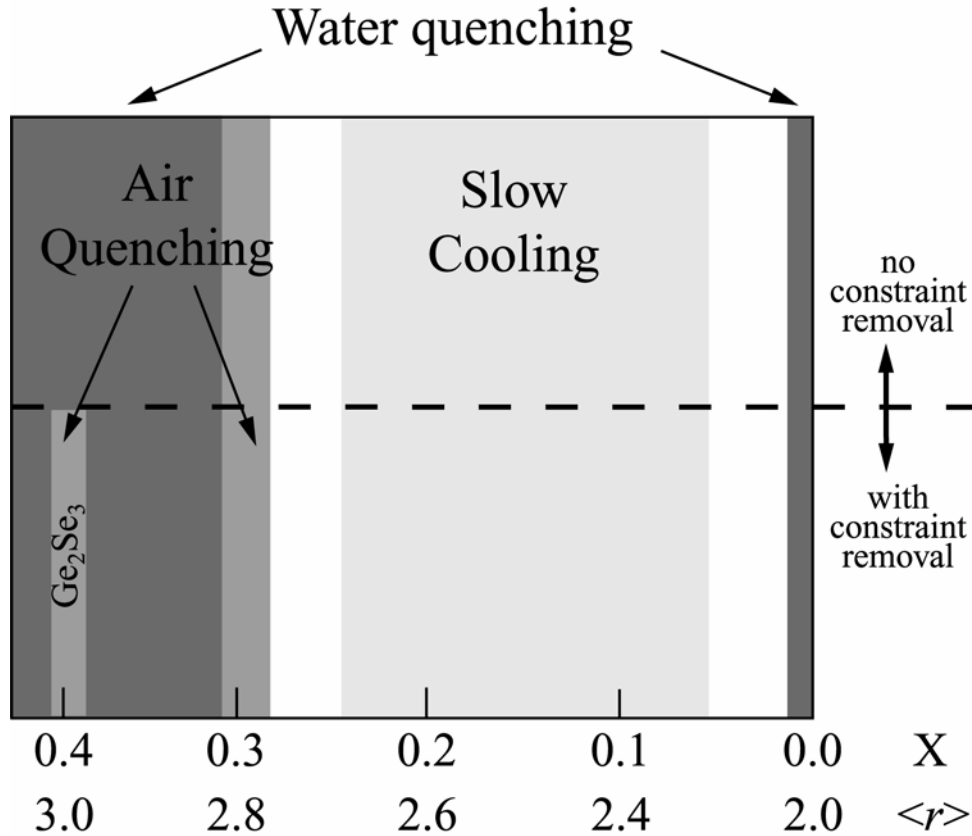


Figure 4.1 – Illustration of the effect of bond constraint removal on glass-forming ability. With no constraint removal, Ge_2Se_3 sits firmly in the water-quenching region. Constraint removal allows the glass to form at lower quench rates.

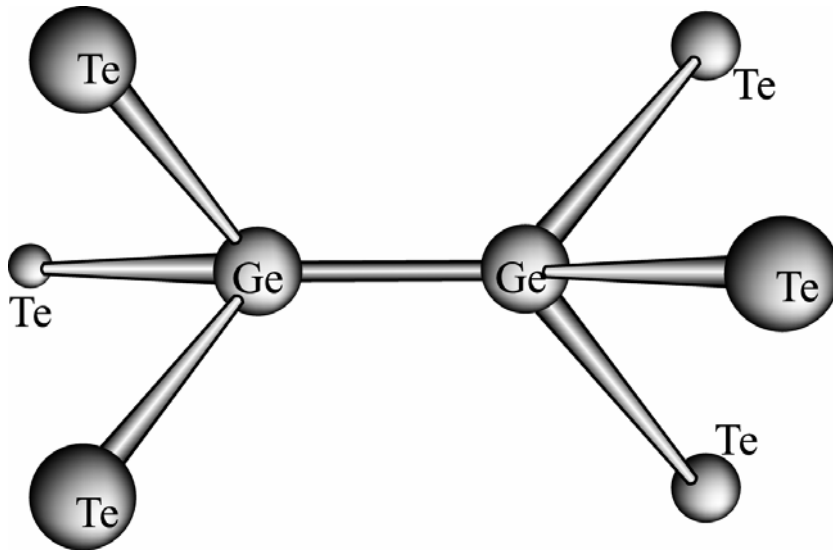


Figure 4.2 – Illustration of the Ge_2Te_3 configuration

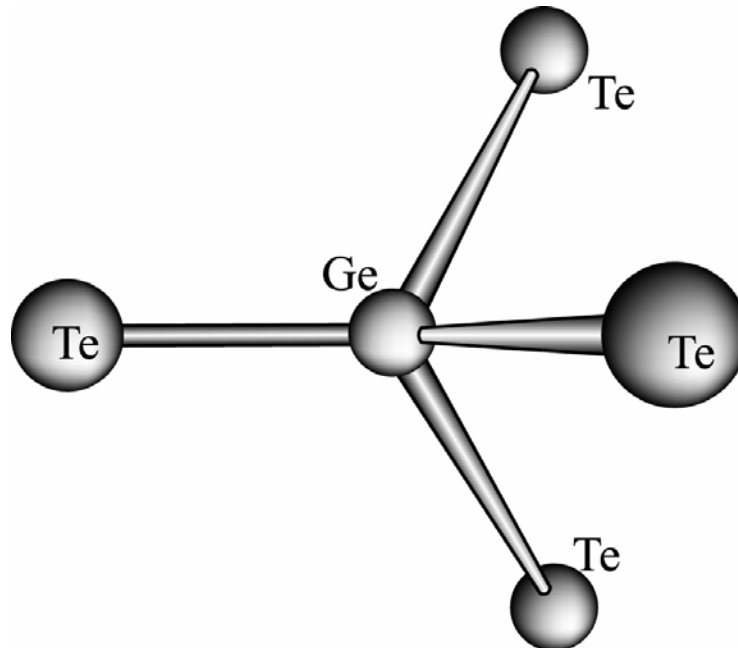


Figure 4.3 – Illustration of the GeTe_2 configuration

4.6 References

Azoulay, R., Thibierge, H., and Brenac, A., *J. Non-Cryst. Solids* **18**, 33 (1975).

Boolchand, P., Lucovsky, G., Phillips, J.C., and Thorpe, M.F., *Phil. Mag.* **85**, 3823 (2005).

Clerk Maxwell, J., *Philos. Mag.* **27**, 294 (1864).

Glasstone, S., Laidler, K.J., and Eyring, H., *The Theory of Rate Processes* (McGraw Hill) 1941.

Kauzmann, W., *Chem. Rev.* **43**, 219 (1948).

Kerner, R., and Phillips, J.C., *Solid St. Commun.* **117**, 47 (2001).

Lagrange, J.L., *Mechanique Analytique*, Paris (1788).

Lucovsky, G. and Phillips, J.C., *Appl. Phys. A* **78**, 453 (2004).

Phillips, J.C., *J. Non-Cryst. Solids*, **34**, 153 (1979).

Zachariasen, W.H., *J. Am. Chem. Soc.* **54**, 3841 (1932).

Zavodsky, M.I., Lei, M., Thorpe, M.F., Day, A.R., and Kuhn, L.A., *Proteins: Struct. Function bioinformatics* **57**, 243 (2004).

Chapter 5 - Phase-Change Alloys and the Ge-Sb-Te System

5.1 Introduction

Major advances punctuate the long and storied past of the study of amorphous semiconductors. For example, Ovshinky's observation of electrical switching in an amorphous chalcogenide alloy heralded an explosion of interest and research in amorphous materials. [Ovshinsky 1968] Shortly thereafter, reports of optical switching in such alloys fueled further interest. [Feinleib et al.] In both the electrical and the optical transitions reported, energy pulses induce phase changes, and pulse duration and magnitude determine the direction of the transition. For an intense pulse that is quickly dissipated, the material melts and then freezes into its glassy state. When energy is delivered less intensely and over a longer period of time, the crystalline state prevails.

In the ensuing decades intense fundamental research deepened understanding of chalcogenide glasses [Adler] and led to considerable technological progress including the demonstration of optical and electronic memory devices. [Takenaga et al.; Neale, et al.] By the early 1990's demonstration of congruent crystallization marked further progress in the study of chalcogenide alloys. [Gonzalez-Hernandez, et al.] In such cases, rapid crystallization occurs with no phase separation, and the amorphous-crystalline transition involves no large-scale atomic motion.

With this prehistory, in recent years alloys in the Ge-Sb-Te system emerged as paradigms of amorphous chalcogenide phase change systems. Using these alloys, applied scientists have now created devices that achieves rapid programming speed and requires very little programming current. [Hudgens and Johnson] Reported programming times decreased

manyfold to tens of nanoseconds in devices scaled to near lithographic limits. [Ovshinsky 1998]

The following reviews some of the previous work on the properties of Ge-Sb-Te alloys, focusing on both advances that led to deeper basic understanding of the alloys as well as on technological developments. Beginning with a discussion of these developments (based largely on a recent review [Hudgens Breckenridge]) the chapter follows with an analysis of the first EXAFS work on these alloys [Kolobov et al.] and considers electronic structure calculations [Robertson et al.] that relate to specific phase-change models based on EXAFS data.

5.2 Phase Change Memory Technology

Chalcogens – group VI elements – typically bond in two-fold coordination that can result in disordered polymeric networks in the liquid state. The resultant increase in viscosity creates a barrier to crystallization and allows – when the cooling kinetics are appropriate – for the liquid system to cool into an amorphous solid state. When cooling is slow enough, on the other hand, atomic reorganization during the cooling process results in a crystalline solid. Figure 5.1 depicts these two processes as an amorphizing RESET pulse and a crystallizing SET pulse. The two states are optically and electrically distinct. To understand this distinction, one must consider the electronic density of states in amorphous and crystalline materials.

In a crystalline semiconductor, an electronic band gap separates the filled valence band states from the unoccupied conduction band states. Mott and – independently – Cohen, Fritzsche and Ovshinsky first described disorder-induced gap states in a model that has come

to be known as the Mott/CFO model. [Mott and Davis; Cohen et al.] In a disordered material in this model, localized electronic states permeate the band gap and cause the Fermi level to be pinned near mid-gap. Carriers in amorphous materials move by hopping between localized states or by trapping into localized states after thermal excitation to extended states. This results in a region in the density of states where mobility is trap-limited, the so-called mobility gap. Within the framework of the Mott/CFO model, a large density of negatively and positively charged traps exist in amorphous chalcogenide semiconductors. These traps behave much like compensating levels in crystalline systems and pin the Fermi level in the middle of the mobility gap. The defects causing these traps occur in pairs, called valence alternation pairs, or VAPs. [Kastner et al.]

For Ge-Sb-Te alloys charge conduction in the crystalline material is bandlike and has a mobility as much as five orders of magnitude more than that in the amorphous state. The resultant room temperature conductivity is typically three orders of magnitude greater in the crystalline state and is p-type and nearly degenerate. The transition between the SET and the RESET states thus relies on atomic motion that changes the long-range order in the system as it switches between the amorphous and crystalline states.

To switch phase-change material between the SET and the RESET states another property of chalcogenide alloys described by Ovshinsky in his seminal paper comes into play: threshold switching. Figure 5.2 schematizes threshold switching. The line starting at the origin with very small slope nearly parallel to the voltage abscissa represents the high resistance RESET state. The line starting at the origin with considerably greater slope indicates a material for which the current increases much more dramatically with voltage, i.e.

the SET or crystalline state. By using a relatively low read voltage as indicated in the figure, one reads the SET and RESET states without switching the material from one state to another. The measured current distinguishes the SET and RESET states.

Application of a larger voltage drives the switch from one state to another. When in the amorphous RESET state, as voltage is increased the current grows linearly until a threshold voltage, V_{th} , is reached at which point the material enters a so-called dynamic ON state. This transient electronic state does not involve a transformation to the low-resistance crystalline state. Rather it entails the filling of charged VAP sites caused by the large electric fields (typically in excess of 10^5 V/cm) characteristic of the dynamic ON state. [Adler et al.] In this state, current is allowed to flow long enough in the SET current regime (see figure 5.2) to convert the material to its crystalline SET state.

To switch the material back to its RESET state, a large current is required as shown in figure 5.2. This RESET pulse must be of large enough magnitude and duration to melt the material, but it must also have a short trailing edge so as to achieve the rapid cooling necessary to lock the sample into the glassy state. Sample volumes can be kept very small thus the RESET pulse can be very short.

Thermal considerations dictate the structures employed in Ge-Sb-Te alloy devices as much as – if not more than – electrical considerations. Early devices possessed relatively large programming volumes and poor thermal efficiency so that programming currents exceeded the upper acceptable limit for commercial technologies. Current devices focus on small programming volumes and optimized thermal environments in order to move towards scalable technologies with appropriate programming currents. Solutions to scaling problems

came only after successful numerical thermal modeling of devices that are complicated by temperature dependencies of electrical and thermal conductivity; percolation in the amorphous-crystalline mixture of device material; and complex crystallization kinetics. [Wicker]

A number of groups have studied the endurance of operational Ge-Sb-Te alloy cells. [Gill, et al.; Lee, et al.] They report between 10^9 and 10^{13} write/erase cycles and identify limits to endurance in terms of delamination of the chalcogenide from the electrode, and changes in the alloy composition due to chemical interactions with the electrode at high temperatures.

5.3 EXAFS Studies of Ge-Sb-Te alloys

Prior to this study, several studies of various chalcogenide alloys existed in the literature. Surprisingly, however, the majority of the EXAFS community took no interest in the Ge-Sb-Te system, the notable exception being Kolobov *et al.* This group published several papers on the subject of $\text{Ge}_2\text{Sb}_2\text{Te}_5$, the most prominent of which featured in Nature Materials in 2004 [Kolobov et al.].

According to this article, EXAFS was carried out on the optically re-crystallized and re-amorphized sections of $\text{Ge}_2\text{Sb}_2\text{Te}_5$ in a “device structure”. Central to the work was the idea that these two phases could be modeled in a new and unique way. The crystalline phase was well-known, given previous X-ray diffraction studies by other groups [Nonaka et al.], so this model is straightforward, and verified by independent research. The amorphous model derived from the crystalline model, requiring only the motion of a significant fraction of the Ge atoms from their crystalline sites featuring octahedral coordination to an “amorphous”

site featuring tetrahedral symmetry via a so-called “umbrella-flip”. The nature of the crystalline model – a distorted rocksalt structure – facilitated this flip motion due to the existence of three weaker ionic-type bonds which, upon laser illumination, were severed, allowing the Ge to move to a more energetically favorable site.

Because EXAFS is a technique that requires the user to fit experimental data to a number of models, it follows that the results then have a tendency to be sensitive to the particular model used in the fit. This analysis, based on an amorphous model which is almost crystalline in nature, shows a bias toward crystallinity in the results. One might ask whether a different model – one that features a more truly random network of Ge, Sb, and Te atoms – applied to the same EXAFS data might have a significantly different, yet equally believable result.

EXAFS is an average spectroscopy, and as such, information derived about a certain sample has atomic specificity, but lacks spatial resolution on the scale that would be required for the amorphous model proffered by Kolobov *et al.* From selected area electron diffraction and tunneling electron microscope measurements [Friedrich *et al.*], it is evident that the laser re-amorphized phase of $\text{Ge}_2\text{Sb}_2\text{Te}_5$ is not necessarily fully amorphous, but is instead slightly micro- or even nano-crystalline. Only with spatial resolution and accuracy on the order of microns or less can one make a valid assumption regarding the heterogeneity of a sample in a device structure based on EXAFS data. It is highly likely that the samples tested previously were a mix of both amorphous and crystalline material, and the EXAFS technique is simply not capable of divining the difference between the two morphologies.

It is for these reasons that EXAFS investigation of $\text{Ge}_2\text{Sb}_2\text{Te}_5$ and other alloys like it must continue. Current assumptions about the particular morphology of phase-change alloys used for devices may not be true, and so, layer by layer, they must be stripped away to ultimately reveal the true nature of the material properties. Kolobov's work, while insightful, makes assumptions that are not valid on the scale that EXAFS can currently see, and his model imposes a certain amount of crystallinity on his EXAFS data, skewing the results for the amorphous material. As will be shown in subsequent chapters, the experiments performed in pursuit of this dissertation avoid both the model-dependant skew as well as the assumption of amorphicity within a device structure.

5.4 Electronic Structure Calculations

Electronic density of states (EDOS) calculations can cast light on conflicting structural models clouded by differing interpretations of atomic structural data. That is, questions involving the atomic structure of Ge-Sb-Te alloys may be addressed by calculating the predicted electronic structure of proposed atomic models and comparing predictions to empirical data. To begin investigation of electronic density of states consider first the Peierls distortion in crystalline (c-) GeTe where the cubic structure with no band gap and all equal bond lengths distorts to an A7 structure. In the latter, each Te and Ge atom has 3 short and 3 long bonds and a band gap opens up as the material distorts. In c- $\text{Ge}_2\text{Sb}_2\text{Te}_5$, or c-GST, a similar Peierls distortion results in all three atomic species having 3 short and 3 long bonds. As demonstrated in the previous section, Kolobov suggests that in the amorphous structure of $\text{Ge}_2\text{Sb}_2\text{Te}_5$, or GST, tellurium atoms form a lattice derived from the cubic phase. [Kolobov et al., 2004] The EXAFS data described in the present work, on the other hand, supports a

structure with lower coordination that includes homopolar germanium bonds. [Baker] Comparison of the predicted electronic properties of GST to experimental data can lead to a resolution of this discrepancy.

Robertson and co-workers [Robertson, et al.] undertook a calculation of the electronic density of states of GST using the ab-initio total energy, plane wave pseudopotential method employing the CASTEP code. [Milman et al.] For the two structures (a- and c-) suggested by Kolobov, the EDOSs for both the a- and c- states calculated by Robertson have a band gap of 0.5 eV. Evidence suggests, however, that the glassy a-GST has a band gap of 0.7 eV. [Kato and Tanaka]

Robertson further points out that his EDOS calculations of a-GST indicate similar weight for all three elements in both the valence band and the conduction band. This suggests that bonding in a-GST is principally covalent and not ionic. He argues – by analogy – that bonding is covalent when GeTe has six bonds of equal length. This also casts doubt on the interpretation of Kolobov.

Arguing by analogy, however, can lead to contradictions. For example, one can investigate trends to compare the structures and bonding of IV-VI compounds. Littlewood found that the more ionic compounds have rock-salt structure. [Littlewood] Materials with a covalent character have a distorted A7 structure. He found GeS and GeSe to be rock-salt while GeTe is A7. Arguing that the structure of a-GeTe and liquid (l-) GeTe should be similar, calculations of the structure of l-GeTe are particularly enlightening. Such calculations indicate A7 structure in the liquid phase. [Raty et al.] Compositional trends thus suggest that in the sulphides and selenides there is more molecular bonding and the 8-N rule

is followed [Lucovsky and White] whereas in a-GeTe – and analogously in a-GST – the 8-N rule is not followed. EXAFS data contradict this conclusion, however. In at least three separate studies, Ge-Ge bonds were seen in a-GeTe. [Kolobov et al., 2003; Maeda and Wakagi; Baker and Sayers] Thus, while arguments describing compositional trends may sometimes be compelling, the evidence here indicates that for the progression from sulfides to selenides to tellurides the trend towards decreasing 8-N rule applicability is not borne out. Analogous arguments for the lack of applicability of the rule for a-GST are not supported by the evidence.

Finally, experimental evidence indicates an energy barrier between a-GST and c-GST of 2.3 eV. [Kalb, et al.; Friedrich et al.] The calculations of Robertson based on the model of Kolobov suggest that the transformation of the Ge site is on the order of 0.4 eV – much lower than that observed. The crystalline and amorphous states must indeed be separated by such a barrier otherwise the glassy phase would, through cycling, convert to the crystal. The lack of a large barrier between the proposed a- and c- states in Kolobov's model casts further doubt on the validity of those models.

5.5 Conclusion

This brief review of some of the published work on the Ge-Sb-Te alloys presents both a discussion of the technological application of these alloys as well as consideration of a previous EXAFS study of $\text{Ge}_2\text{Sb}_2\text{Te}_5$. Analysis of the latter in light of independent electronic structure calculations suggests that the modifications associated with phase changes in these alloys are not well understood. A careful analysis of the atomic structure of $\text{Ge}_2\text{Sb}_2\text{Te}_5$ may lead to a deeper understanding of – and hopefully enhanced technological

exploitation of – this exciting phase change alloy. A discussion of just such an EXAFS study begins in the following chapter.

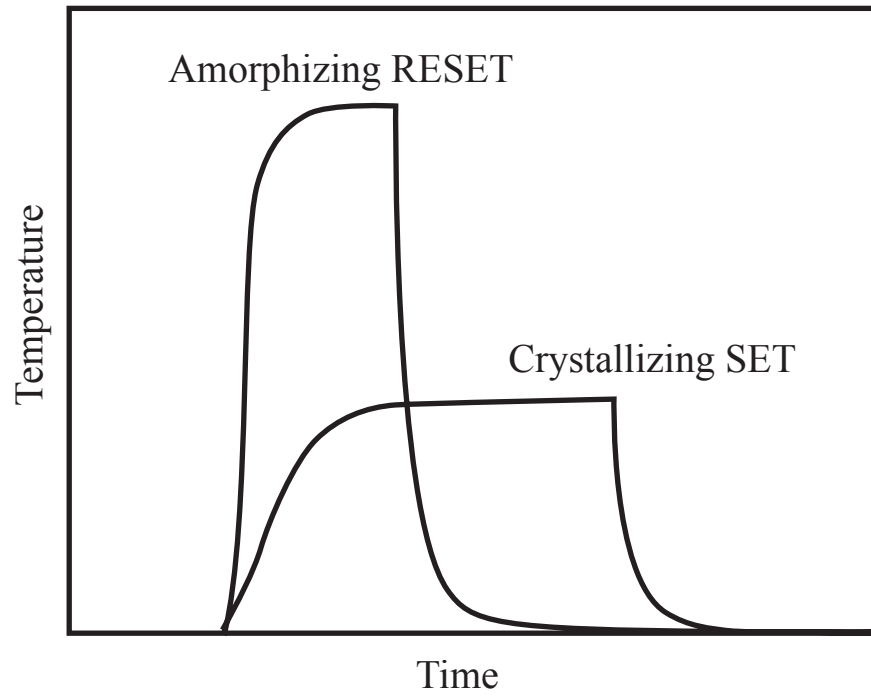


Figure 5.1 – Illustration of the optical switching mechanism of phase-change materials. The SET pulse heats the material to just above the crystallization temperature, while the RESET pulse melts the material and quenches quickly.

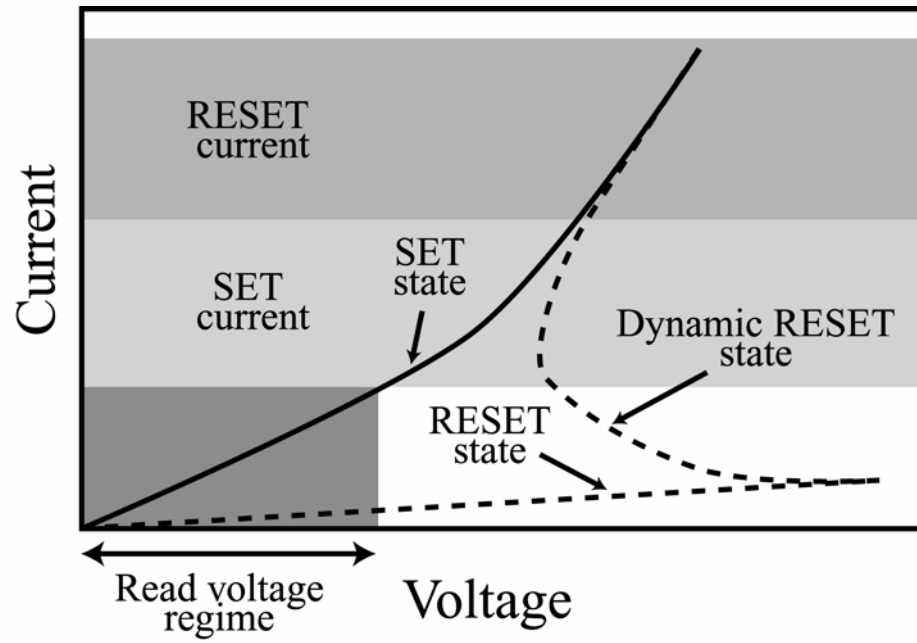


Figure 5.2 – The I-V characteristic of phase-change materials.

5.6 References

- Adler, D., Scientific American, **236**, 36 (1977).
- Adler, D., Shur, M.S., Silver, M., and Ovshinsky, S.R., J. Appl. Phys. **51**, 3289 (1980).
- Cohen, M.H., Fritzsche, H., and Ovshinsky, S.R., Phys. Rev. Lett. **22**, 1065 (1969).
- Baker, D.A., Paesler, M.A., Lucovsky, G., Agarwal, S.C., and Taylor, P.C., Phys. Rev. Lett. **96**, 255501 (2006).
- Baker, D.A. and Sayers, D.E., unpublished 2003.
- Feinleib, J., de Neufville, J., Moss, S.C., and Ovshinsky, S.R., Appl. Phys. Lett. **18**, 254 (1971).
- Friedrich, I., Weidenhof, V., Lenk, S., and Wuttig, M., Thin Solid Films **389**, 239 (2001).
- Gill, M., Lowrey, T., and Park, J., ISSCC 2002 Tech, Dig., paper no. 12.4 (2002).
- Gonzalez-Hernandez, J., Chao, B.S., Strand, D., Ovshinsky, S.R., pawlik, D., and Gasiorowski, P., Appl. Phys. Comm. **11**, 557 (1992).
- Hudgens, S., and Johnson, B., MRS Bulletin, November 2004, p. 1.
- Kato, T, and Tanaka, K., Jpn. J. Appl. Phys. **44**, 7340 (2005).
- Kastner, M., Adler, D., and Fritzsche, H., Phys. Rev. Lett. **37**, 1504 (1976).
- Kolobov, A.V., Tominga, J., Fons, P., and Uruga, T., Appl. Phys. Lett. **82**, 382 (2003)
- Kolobov, A., Fons, P., Frenkel, A.I., Ankudinov, A.L., Tominaga, J., and Uruga, T., Nature Mater. **3**, 703 (2004).
- Lee, S.H., Hwang, Y.N., Lee, S.Y., Ryoo, K.C., Ahn, S.J., Koo, H.C., Jeong, C.W., Kim, Y.T., Koh, G.H., Jeong, G.T., Jeong, H.S., and Kim, K., in 2004 Symp. On VLSI Technol. Dig. Tech. Papers, 20 (2004).

- Littlewood, P.B., J. Phys. C **13**, 4855 (1980).
- Lucovsky, G., and White R.M., Phys. Rev. **B8**, 660 (1973).
- Maede, Y., and Wakagi, M., Jpn. J. Appl. Phys. **30**, 101 (1991).
- Mott, N.F., and Davis, E.A., *Electronic Process in Non-Crystalline Materials* (Oxford University Press, 1971).
- Neale, R.G., Nelson, D.L., and Moore, G.E., Electronics, September 1970, p. 56.
- Nonaka, T., Ohbayashi, G., Toriumi, Y., Mori, Y., and Hashimoto, H., Thin Solid Films **370**, 258 (2000)/
- Ovshinsky, S.R., Phys. Rev. Lett. **21**, 1450 (1968).
- Ovshinsky, S.R., IEEE Proc. CAS 1 (Institute of Electrical and Electronics Engineers, Piscataway, NJ) p. 33.
- Raty, J.Y., Godlevsky, V.V., Ghosez, P., Bichara, C., Gaspard, J.P., and Chelikowsky, J.R., Phys. Rev. Lett. **85**, 1950 (2000).
- Robertson, J., Xiong, K., and Peacock, P.W., Thin Solid films **515** 7538 (2007).
- Takenaga, M., Yamada, N., Ohara, S., Nishiuchi, K., Nagasima, M., Kashihara, T., Nakamura, S., and Yashimata, T., Proc. SPIE **420**, 173 (1983).
- Wicker, G., "A Comprehensive Model of Subicron Chalcogenide Switching Devices," PhD dissertation, Wayne State University, Detroit, MI 1996.

Chapter 6 - EXAFS Theory and Application

6.1 Introduction

In the study of amorphous materials, a probe of the local environment is key to understanding the intricate internal atomic interplay. This is especially true in the case of phase-change materials, from which the Ge-Sb-Te system stands out as the focus of both intense study [Friedrich et al.; Karpinski et al.; Yamada and Matsunaga] and industrial application [Yinug]. Given these conditions, a particularly useful probe of local structure is found in Extended X-ray Absorption Fine Structure (EXAFS) spectroscopy, a technique with roots going back almost a century. In the last 40 years, however, what was once a laboratory curiosity has blossomed into a thriving method of scientific inquiry, now incorporating dozens of multi-billion-dollar dedicated synchrotron light source facilities around the globe, attended by thousands of workers, technicians, Ph.D.s, and students alike. EXAFS spectroscopy's ability to probe not only the local atomic structure of amorphous materials - but the *species-specific* structure *directly* - gives it an edge over other spectroscopies such as Raman or infra-red. This chapter includes a brief history of EXAFS spectroscopy, with relevant theoretical and experimental considerations, and an explanation of the specific experimental setup and sample preparation required to probe the Ge-Sb-Te alloys under investigation.

6.2 A Short History of EXAFS

Beginning with Hugo Fricke's [Fricke] and Gustav Hertz' [Hertz] experimental observation of oscillations in the absorption coefficient at energies above the primary absorption edge, x-ray absorption fine structure (XAFS) has enjoyed a rich and varied

history. The following years brought several attempts at theoretical explanation, notably Kronig's attempt at a long-range order (LRO) theory [Kronig 1931] based on the gaps in energy at the Brillouin zone boundaries. Kronig was forced to confront observations of fine structure in both crystallites, with order that was decidedly long-range and therefore fit into his theory, and molecules, which lacked significant long range order and thus fell outside the boundaries of his theory. This inadequacy of LRO theory looming, Kronig developed a short-range order (SRO) theory, based on scattered waves from a point source [Kronig 1932]. In spite of experimental advances [Peterson; Kostarev; Sawada; Schmidt], conflict continued regarding the accuracy of these theories, until in 1962, measurements made by Nelson, Siegel, and Wagner [Nelson, Siegel, and Wagner] confirmed the qualitative accuracy of SRO theory. Eight years later, Sayers, Lytle, and Stern published a comprehensive point-scattering SRO theory of EXAFS [Sayers, Lytle, and Stern], followed one year later by the successful application of that theory to Fe, Cu, and Ge spectra [Sayers, Stern, and Lytle]. This served as the final nail in the coffin of LRO theory, and, simultaneously, the transformation of EXAFS from a scientific curiosity into a quantitative tool for structure determination at the atomic level. Since 1970, advances in XAFS-related technology have accelerated, leading researchers to push the envelope of data collection, data analysis, range and focus of experimental techniques, and overall accessibility to the technique itself. Now, a third generation of dedicated synchrotron light sources holds even more promise of advancement in the field, with new discoveries just around the corner.

Because EXAFS is fundamentally a short range order probe, it is well-suited to examine amorphous materials; a class of materials that has historically taken a back seat to

the more readily understood crystalline phases. Now, however, EXAFS occupies a well-established niche in the scientific community, and results from its use have made a significant contribution to the re-emergence of the amorphous semiconductor as the subject of heightened interest.

6.3 EXAFS Theory

EXAFS is a spectroscopy based on the absorption of x-ray photons of sufficiently high energy to eject a core electron from an absorbing atom. The subsequent photoelectron wave packet has a kinetic energy

$$E_k = h\nu - E_b \quad (6.1)$$

where the incoming x-ray of frequency ν has an energy $h\nu$ and E_b is the binding energy of the core electron. The notation convention used here is that of Siegbahn, designating electrons in the $n = 1$ shell (1s state) as K electrons, those in the $n = 2$ shell (2p states) as L electrons, and so on. The corresponding absorption edges are named accordingly.

In general, an x-ray beam of intensity I_0 passing through a sample of thickness d is attenuated, and the transmitted intensity I is given by the Beer-Lambert law:

$$I = I_0 e^{-\mu(E)d} \quad (6.2)$$

In the dipole approximation [Schift], the photoelectron absorption $\mu(E)$ to first order in the field is given by [Bethe]

$$\mu(E) = \frac{4N_0\pi^2 e^2 \omega}{c} \langle f | \boldsymbol{\varepsilon} \cdot \mathbf{r} | i \rangle^2 \rho(E_f), \quad (6.3)$$

where N_0 is the number of absorber atoms per unit volume, ω is the angular frequency of the incoming photon, $|i\rangle$ is the initial state wave function of the bound electron, $|f\rangle$ is the

final state wave function of the ejected electron, and $\rho(E_f)$ is the density of the allowed states at the final state energy E_f . $\boldsymbol{\varepsilon}$ is the electric field polarization vector of the x-ray photons, e is the electron charge, and c is the speed of light.

For x-ray energies near an absorption edge, several physical effects contribute to the structure of the spectrum, such as core electron transitions to unoccupied bound states and low-lying continuum states, or multiple scattering effects that arise from angular arrangement of the atoms in the nearby environment of the absorbing atom. This region near the edge is named either X-ray Absorption Near Edge Structure (XANES) or, in the soft x-ray, molecular, and surface spectroscopy communities, Near Edge X-ray Absorption Fine Structure (NEXAFS) [Bianconi; Stöhr]

For x-ray energies greater than ~ 40 eV above an absorption edge, $\rho(E_f)$ gives a monotonic contribution to the absorption coefficient. EXAFS must arise, then, from the matrix element term $\langle f | \boldsymbol{\varepsilon} \cdot \mathbf{r} | i \rangle^2$. Because the initial state wave function is unchanging, the structure is found in the final state wave function. In any condensed matter subject to impinging x-rays, ejected core electrons scatter off of the surrounding atoms, and the final state wave function is a superposition of both the outgoing wave function, $|f\rangle_{outgoing}$, and the backscattered wave function, $|f\rangle_{backscattered}$. The nature of these wave functions is such that constructive or destructive interference gives rise to oscillatory variation in the matrix element as a function of ω . In this same regime, and incorporating moderate thermal or static disorder, this modulation (χ) of the absorption coefficient, normalized to the ‘background’ absorption (μ_0), can be expressed as

$$\chi(k) = \frac{\mu(k) - \mu_0(k)}{\mu_0(k)}, \quad (6.4)$$

where the wavevector of the ejected photoelectron is given by the familiar equation

$$k = \sqrt{\frac{2m_e}{h^2}(h\nu - E_b)}. \quad (6.5)$$

For an unoriented sample with Gaussian disorder, and incorporating many-body effect corrections, the EXAFS in the single scattering approximation can be expressed as [Sayers, Lytle, and Stern; Stern 1974, Kincaid and Eisenberger, Lee and Pendry, Lee and Beni]

$$\chi(k) = \sum_j N_j S_{0i}^2(k) F_j(k) e^{-2\sigma_j^2 k^2} e^{-\frac{2r_j}{\lambda(k)}} \frac{\sin(2kr_j + \phi_j(k))}{kr_j^2}. \quad (6.6)$$

Here $F_j(k)$ is the backscattering amplitude from each of the N_j neighboring atoms of the j^{th} type a distance of r_j away. $\phi_j(k)$ is the total phase shift experienced by the photoelectron. The term $e^{-\frac{2r_j}{\lambda(k)}}$ is due to inelastic losses (from neighboring atoms and the inter-atomic medium) in the scattering process with $\lambda(k)$ representing the electron mean free path as a function of k . [Rehr et al.; Stern, Heald, and Bunker; Stern and Rehr, Teo and Lee] $S_{0i}^2(k)$ is the amplitude reduction factor due to many-body effects at the central atom (denoted by i), such as a shake up process, where one or more electrons are excited to varying unoccupied bound states, or a shake off process, where electrons are ejected from the atom entirely. Finally, the $e^{-2\sigma_j^2 k^2}$ term includes σ_j , the so-called Debye-Waller factor, a term that accounts for thermal vibration (in the harmonic approximation) and static disorder (assuming Gaussian pair distribution).

This equation defines the EXAFS signal as a modification of the backscattering amplitude $(N_j F_j(k))$ by the reduction factors $S_{0i}^2(k)$, $e^{-2\sigma_j^2 k^2}$, and $e^{-\frac{2r_j}{\lambda(k)}}$, a $1/kr_j^2$ distance dependence, and a sinusoidal oscillation which is a function of interatomic distances $(2kr_j)$ and photoelectron phase shifts $(\phi_j(k))$.

With the regular assumptions, the Debye-Waller term is given by

$$\sigma_{total}^2 = \sigma_{static}^2 + \sigma_{vibrational}^2, \quad (6.7)$$

where the static disorder term is

$$\sigma_{static}^2 = \frac{\sum_{j=1}^N \frac{r_j^2 - r_0^2}{N}}{N} \quad (6.8)$$

and the vibrational term is

$$\sigma_{vibrational}^2 = \frac{h}{8\pi^2 \nu \mu} \cot\left(\frac{h\nu}{2kT}\right), \quad (6.9)$$

assuming harmonic vibrations in the Einstein model approximation. Here, μ is reduced mass, T is temperature, and ν is the bond-stretching vibrational frequency. It is important to note that the vibrational Debye-Waller term that enters into EXAFS is not the same as that which enters into diffraction. In diffraction, the vibrational term refers to mean square deviations of atoms with respect to their respective lattice sites, while for EXAFS the term refers to the relative deviation between the absorbing and backscattering atoms.

The sinusoidal term, $\sin(2kr_j + \phi_j(k))$, includes information that gives the phase difference between the outgoing and incoming (backscattered) portions of the photoelectron wave function. The first term indicates that the backscattered photoelectron wave is phase

shifted by $2kr_j$ because it travels from the absorbing atom to the neighboring atom j and back. The second term incorporates two additional phase shifts, one from the potential of the absorbing atom (experienced twice); $2\delta(k)$, and one from the potential of the j^{th} neighboring atom; $\theta_j(k)$. The second term is then $\phi_j(k) = 2\delta(k) + \theta_j(k)$.

The Debye-Waller term is significant in that its assumptions are violated when considering materials with a large amount of disorder, as in this study. Asymmetric pair correlation functions in the static term or anharmonic vibration potential are important factors for highly amorphous materials, superionic conductors [Boyce and Hayes], and liquid metals [Crozier and Seary]. Neglecting these effects can result in an apparent decrease in the reported interatomic distances and coordination numbers as well as the possible misidentification of nearest neighbor species. [Martens et al.; Crozier; Eisenberger] These effects are taken into consideration in current theory and analysis techniques, but are mentioned here for completeness.

One can easily see that structural information is explicit in equation 6.6, hereafter referred to as the EXAFS equation. A detailed picture of the local structure is accessible with EXAFS spectroscopy, and this includes information about interatomic distances, coordination numbers, atomic species, and thermal vibration and static disorder. EXAFS theory and applications continue to advance and grow, and several resources are available that provide thorough background, review, and discussion. [Rehr and Albers; Filipponi] In addition, the most current and complete treatments on the subject can be found online at <http://xafs.org/>.

6.4 Synchrotron Light Sources

EXAFS spectroscopy requires high-intensity radiation in the hard x-ray region of the EM spectrum. In addition, the x-rays must be monochromatic as well as tunable, so as to enable a monotonic sweep in energy from low to high, (or *vice-versa*). In the early days of x-ray absorption spectroscopy (XAS), teams of scientists worked parasitically off of existing cyclotron particle accelerators, where synchrotron radiation was first observed. Eventually, the United States Department of Energy's Office of Basic Energy Sciences recognized the need for dedicated sources of high-energy light with the requirements noted above, and the so-called "second generation" of synchrotron light sources became a reality in the late 1970s and early 1980s. In the late 1990s and early 2000's, third generation synchrotrons came online with brighter, more tightly collimated beams and higher range of available energies for research. At the time of this writing, experimenters and engineers continue to push the envelope of current technology into the future, where lies the fourth generation light sources. These sources are based on linear accelerators and free electron lasers, with high coherence and short pulse duration dominate the design specifications. More information regarding synchrotron sources can be found online at <http://www.lightsources.org/cms/>.

6.4.1 Synchrotron Light

While the basic equations describing synchrotron radiation are given in detail in several sources [Schwinger; Sokolov and Ternov; Godwin; Jackson], and detailed treatments on the subject are available elsewhere [Bachrach; Kock; Margaritondo], a brief introduction is given here for completeness. This section gives a short technical overview of the

Advanced Photon Source synchrotron and the ID-10 beamline used to gather the data for this body of work.

It is well known that an accelerating charge radiates energy in the form of photons. When the speed of the accelerating charge is much less than the speed of light, -i.e. non-relativistic-, the angular distribution of the radiation is that of a dipole. As the charge moves faster and approaches relativistic speeds, the angular distribution tips sharply forward in the direction of motion. In a synchrotron, the motion of the charged particles is circular, thus the radiation sweeps out a “searchlight” pattern, as shown in figure 6.1. The inclusion of insertion devices such as wigglers or undulators results in additional intensity and a wider frequency distribution. Synchrotron radiation produced at a typical third-generation facility such as the Advanced Photon Source (APS) at Argonne National Laboratories exhibits a wide spectral range, including photon energies from infrared to hard-x-ray. Intensities at the APS are four or more orders of magnitude greater than those of tube sources. In addition the radiation is highly collimated and pulse durations are on the order of nanoseconds or less. The spectral distribution for the APS in comparison to other x-ray sources is shown in figure 6.2. The characteristics listed here allow not only the successful collection of EXAFS data, but collection of high-quality spectra over a broad range of atomic species and morphologies.

6.4.2 Beamline and Experimental Setup

At the time of this writing, the APS houses 34 operational beamlines, with 67 experimental stations, each of which operate almost continuously for nine months out of the typical year. The Materials Research Collaborative Access Team (MR-CAT), a multiple-institution consortium operates beamline number ID-10 at the APS, where the experimental

work for this dissertation was performed. In order to perform an EXAFS experiment, the incident X-rays must be monochromatic and tunable. Because of the penetrating nature of X-rays, a glancing-angle monochromator is necessary for frequency selection. According to the MR-CAT website [http://mrcat.iit.edu/mrcat_instrumentation.html], the ID-10 line uses

“a Si (111) monochromator consisting of a cryo-cooled first crystal designed by the [Illinois Institute of Technology] Center for Synchrotron Radiation Research and Instrumentation (CSRRI) and a 250mm long second crystal which provides an energy range of 4.8keV to 30keV from the fundamental reflection. Both crystals have been chemically polished and have been measured to deliver the theoretical photon flux to the experimental station. The second crystal has a piezoelectric tuning actuator with a.c. feedback and a Bragg-normal motion which permits some degree of fixed-offset operation.”

In practice, this beamline routinely achieves energies of up to 35keV [Segre]. The resolution of the monochromator is $\Delta E/E = 1 \times 10^{-4}$ [ID-10 website], allowing for refined EXAFS measurements and improved parameter determination.

Every beamline has the same basic layout for an experiment. X-rays pass from the insertion device through a collimating mirror followed by a set of beam monitors and safety slits. From these, the remaining photons pass through the monochromator and enter the experimental station. The geometry of an EXAFS experiment is linear, requiring the placement of only three objects in the path of the x-rays, as shown in figure 6.3. The first is an ion chamber, labeled I_0 , which measures the intensity of the incident beam. The second is the sample to be measured. The third is a second ion chamber, labeled I_t , which measures the intensity of the beam after absorption has occurred. An optional set of downstream objects are a standard sample (similar in composition to the unknown sample, but with known

parameters) and an ion chamber, labeled I_{ref} , which measures the intensity of the beam after absorption by the standard.

An ion chamber measures beam intensity indirectly. X-rays passing through the detector interact with the gas(es) contained therein to produce fast photoelectrons, Auger electrons, and/or fluorescence photoelectrons. These interactions cause gas ionization, so when a voltage is applied to the chamber, the ions and electrons are drawn apart prior to recombination. The resulting voltage is proportional to the number of photons absorbed. This proportionality is not always linear, but given the proper gases and applied voltage, linearity can be achieved over the energy range of the EXAFS scan, typically between 800 eV and 1300 eV above the absorption edge.

Around the absorption energy of germanium's K edge, 11103 eV, an ion chamber 30 cm long containing only nitrogen will absorb about 8% of the photons passing through it. This is ideal for an I_0 chamber, where enough photons are absorbed to give a signal, yet the bulk of the beam impinges on the sample. Sixty percent argon and 40% nitrogen fills the I_t and I_{ref} chambers, resulting in about 75% absorption. The higher absorption energies of antimony and tellurium require a mixture of 15% krypton to 85% nitrogen for the I_0 chamber and 100% krypton for the I_t chamber. The signals from these chambers are collected and saved in a text file on the control computer for later analysis.

6.5 Sample Preparation

EXAFS as a physical phenomenon places few limits on sample type or morphology. All matter attenuates x-rays, and because that phenomenon theoretically only requires a few atoms to occur, the size of the sample is limited only by the measurement technique itself. In

reality, however, the beamline geometry and detector scheme outlined above impose stricter limits on the sample.

In order to measure a signal in the I_t chamber, a sufficient number of photons must make it through the sample. Consider equation 6.2. A “sufficient number of photons” is seen when the ratio $I/I_0 \approx 1/e$. This means that for ideal absorption *in transmission*, the quantity $\mu d \approx 1$. Because the absorption coefficient μ is the measurable quantity, it follows that there exists an ideal sample thickness d . Also, because μ is a function of energy, the ideal thickness is also a function of energy. For a sample of mixed composition such as GST, the ideal thickness of the whole is an average of the ideal thicknesses of the constituent parts. It is important to note that because the ideal thickness varies from energy to energy and material to material, the result of these calculations should serve only as a “rule of thumb” for creating samples. Calculations indicate that maximum ideal thickness of $\text{Ge}_2\text{Sb}_2\text{Te}_x$ lies between about 15 μm at the Ge edge, 110 μm at the Sb edge, and 53 μm at the Te edge.

These differing absorption lengths present a problem; i.e. sufficient absorption at the Sb edge requires a much thicker sample than for the Ge edge. If a thicker sample were used to accommodate the Sb ideal absorption, there would be far too much attenuation at the Ge edge. Alternatively, if a thin sample were used to accommodate the Ge ideal absorption, there would be no signal at the Sb edge. To overcome this challenge, Ge-Sb-Te samples supplied by collaborators at the University of Utah were RF sputtered onto an aluminum foil substrate at a thickness of about 2 μm . The foil was then folded over itself 4, 7, and 6 times

for the Ge, Sb, and Te edge measurements, creating effective sample thicknesses of 16 μm , 128 μm , and 64 μm , respectively.

Because the absorption length of aluminum is much longer than that of Ge, Sb, or Te, it is essentially transparent to the impinging photons. The x-rays absorbed by the substrate scale slowly with energy, and their contributions to the EXAFS signal are easily removed.

6.6 Data Analysis

Beginning about 50 eV above the absorption edge and on top of the slowly varying absorption background lies the usable data in an EXAFS spectrum. Before extracting any material parameters from the data, the data itself must be extracted from the raw spectrum. This process is well-established [Sayers and Bunker; Newville, *et al*; Hayes and Boyce], and implemented in several software packages [Ravel and Newville, Newville] freely available online. This section gives an overview of the techniques of data processing and analysis used in the study of Ge-Sb-Te alloys.

6.6.1 Background Removal

The Athena EXAFS processing software, written by Bruce Ravel [Ravel and Newville], is a front end for the IFEFFIT software package [Newville]. In concert, these two programs facilitate all necessary steps to successfully process raw EXAFS data. Figure 6.4 shows the raw EXAFS data at the Ge edge of the amorphous $\text{Ge}_2\text{Sb}_2\text{Te}_5$ sample. The background of the data generally slopes downward, and both pre-edge and post-edge contributions must be removed. Pre-edge removal consists of fitting a linear spline to two points in that region, which extends above the edge. The post-edge spline is a quadratic fit to two points in that region. Both splines are then subtracted from the data, resulting in a

“background absorption” curve $\mu_0(E)$. This background absorption is then normalized to the edge step, i.e. the difference between the pre-edge and post-edge lines at the absorption edge, E_0 .

Further background removal is an iterative process involving a single low-order polynomial fit over the whole range of data, EXAFS data fitting, and orthogonal polynomial fitting.

6.6.2 E to k Conversion and Weighting

Following normalization, EXAFS data must undergo conversion from energy space E to momentum space k according to

$$k = \sqrt{\frac{2m}{\hbar^2}(E - E_0^{\text{exp}})}, \quad (6.10)$$

where E_0^{exp} is the experimentally determined absorption edge, typically chosen to coincide with the maximum of the second derivative.

A weighting scheme of k^3 compensates for the attenuation in EXAFS amplitude at higher k values, and prevents the domination of larger amplitude oscillations in determination of interatomic distances. In addition, this weighting scheme minimizes the influence of chemical and multiple scattering effects on the signal, which occurs mainly in the low- k region of the spectrum.

6.6.3 Fourier Transform

In order to visualize the data in real space, a Fourier transformation is taken over a range of k_{min} to k_{max} , resulting in a modified radial distribution function

$$\rho(r') = \frac{1}{(2\pi)^{1/2}} \int_{k_{\min}}^{k_{\max}} w(k) k^3 \chi(k) e^{i2kr'} dk. \quad (6.11)$$

where $w(k)$ is a window function designed to reduce truncation artifacts in the transform.

The $w(k)$ used in this study was a Hanning window, defined by

$$w(k) = \frac{1}{2} \left[1 - \cos(2\pi) \cdot \left(\frac{k - k_{\min}}{k_{\max} - k_{\min}} \right) \right]. \quad (6.12)$$

Figure 6.5 shows the Ge EXAFS spectrum normalized, converted to k space, and weighted by the k^3 factor following the iterative background removal process. The dashed line shows the Hanning window, scaled to better represent the multiplicative effect on the data. Figure 6.6 shows the modified radial distribution function of that same Ge data.

6.6.4 Inverse Fourier Transform

From figure 6.6, it is evident that there is one dominant peak. This peak holds the desired information about a single shell in the local structure. To get useful information from that data, and that data alone, an inverse Fourier transform is performed over the window from R_{\min} to R_{\max}

$$k^3 \chi_j(k) = \frac{1}{(2\pi)^{1/2}} \int_{R_{\min}}^{R_{\max}} w(r) \rho(r) e^{-i2kr} dr \quad (6.13)$$

where $w(R)$ is again the Hanning window function, modified for R-space. Both real and imaginary parts comprise this back-transformed function, containing phase - $\phi_j(k) = \arctan[\text{Im}(k)/\text{Re}(k)]$ - and amplitude - $A_j(k) = \sqrt{\text{Im}^2(k) + \text{Re}^2(k)}$ - information.

From the EXAFS equation the amplitude is given by

$$A_j(k) = \frac{N_j}{kr_j^2} S_{0j}^2(k) F_j(k) e^{-2\sigma_j^2 k^2} e^{-\frac{2r_j}{\lambda(k)}} \quad (6.14)$$

while the phase is give by

$$\phi_j(k) = 2kR_j + \delta_j(k). \quad (6.15)$$

With the background removed, the data normalized, the E-to- k conversion performed, and the Fourier transform taken, Artemis' work is done, and the task of extracting structural parameters can begin.

6.6.5 Determination of Structural Parameters

In addition to the Artemis software package, Bruce Ravel has written Artemis, the complimentary data analysis package [Ravel and Newville]. Artemis, like its data processing counterpart, is a front-end for the IFEFFIT software package, the former providing an intuitive, user-friendly interface for the command-line style of the latter. Both of these packages utilize the FEFF simulation code,

“...an automated program for ab initio multiple scattering calculations of X-ray Absorption Fine Structure (XAFS) and X-ray Absorption Near-Edge Structure (XANES) spectra for clusters of atoms. The code yields scattering amplitudes and phases used in many modern XAFS analysis codes, as well as various other properties.” [Rehr et al.]

At a basic level, a FEFF simulation parameterizes the EXAFS equation. Varying these four parameters, R , N , σ^2 , and E_0 , and performing an iterative non-linear least-squares fitting algorithm against the experimental data serves as a reliable and powerful method of parameter determination.

The fitting algorithm minimizes the squares of the residuals

$$\Delta = \sum_i [k^n \chi(k) - Y(k)]^2 \quad (6.16)$$

where $Y(k)$ represents the parameterized theory, and Δ runs through all i data points. There are drawbacks to this method, and they must be accounted for in any analysis. The major drawbacks are parameter correlations and false minima. It turns out that the two sets of parameters - $\{F(k), \sigma, \lambda, N\}$ and $\{p(k), E_0, R\}$ – often contain significant correlations both within and between the sets. High correlations can lead to an artificially good fit, giving inaccurate results. Beginning the analysis with educated guesses about the parameters or pinning certain parameters to known physical values during the fit increases the likelihood of success for this method. False minima occur regularly, and generally, incorporating some *a priori* knowledge of the system into the parameters helps to circumvent this pitfall.

The following chapter details the results of the EXAFS technique outlined above applied to alloys in the Ge-Sb-Te system.

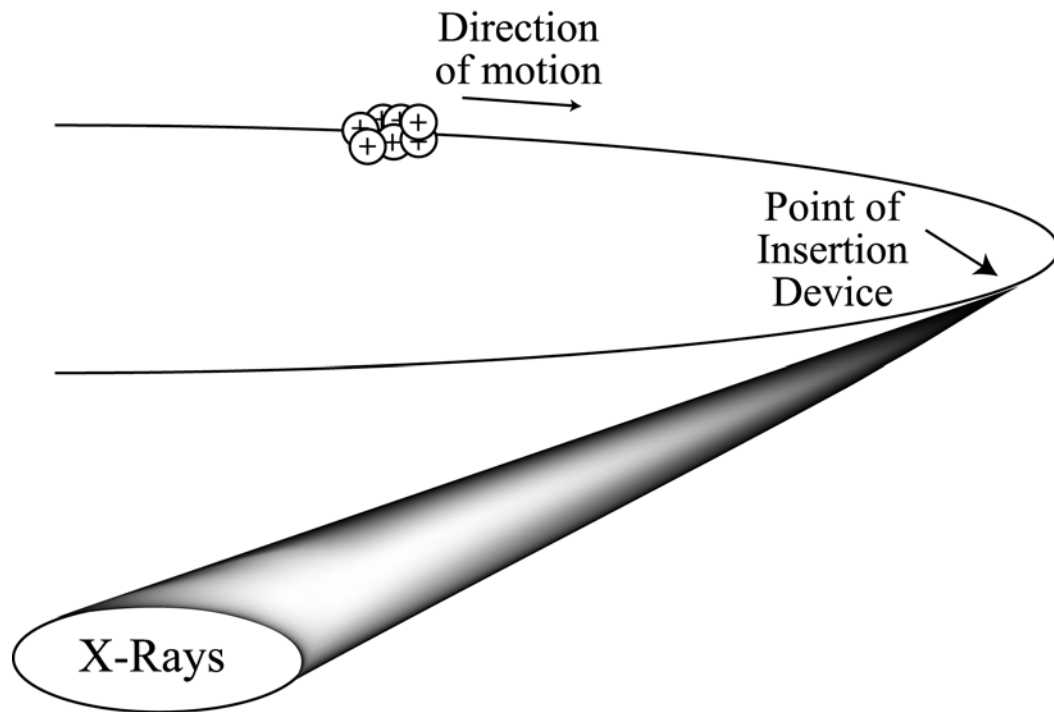


Figure 6.1 – Schematic of synchrotron radiation illustrating the “searchlight” pattern formed by rotating charge packets.

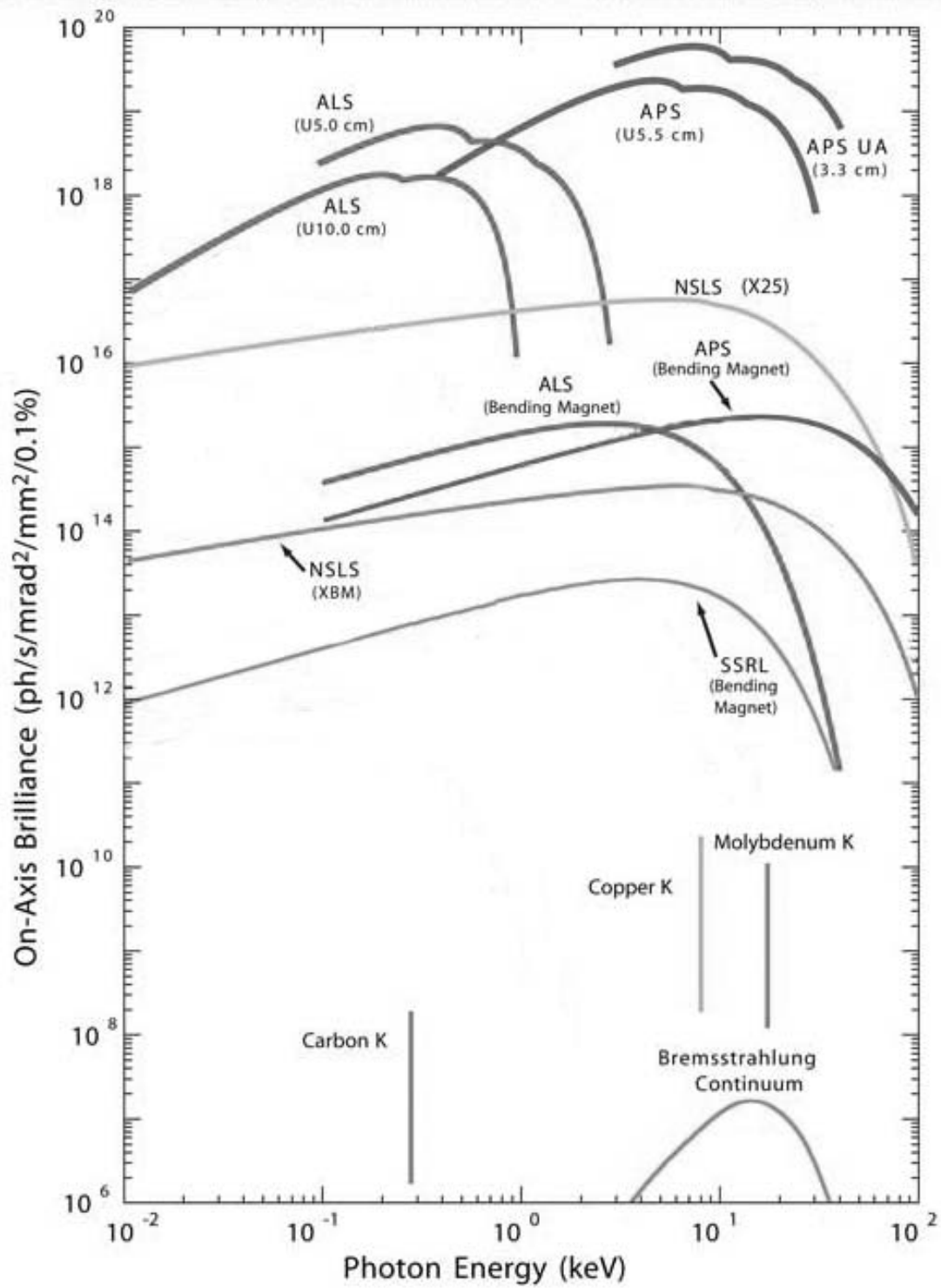


Figure 6.2 – Plot of photon energy vs. on-axis brilliance for various x-ray sources.

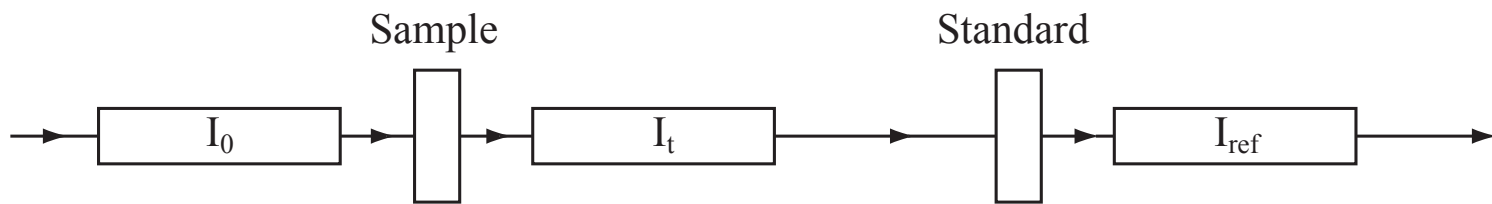


Figure 6.3 – Schematic of a typical EXAFS experimental setup.

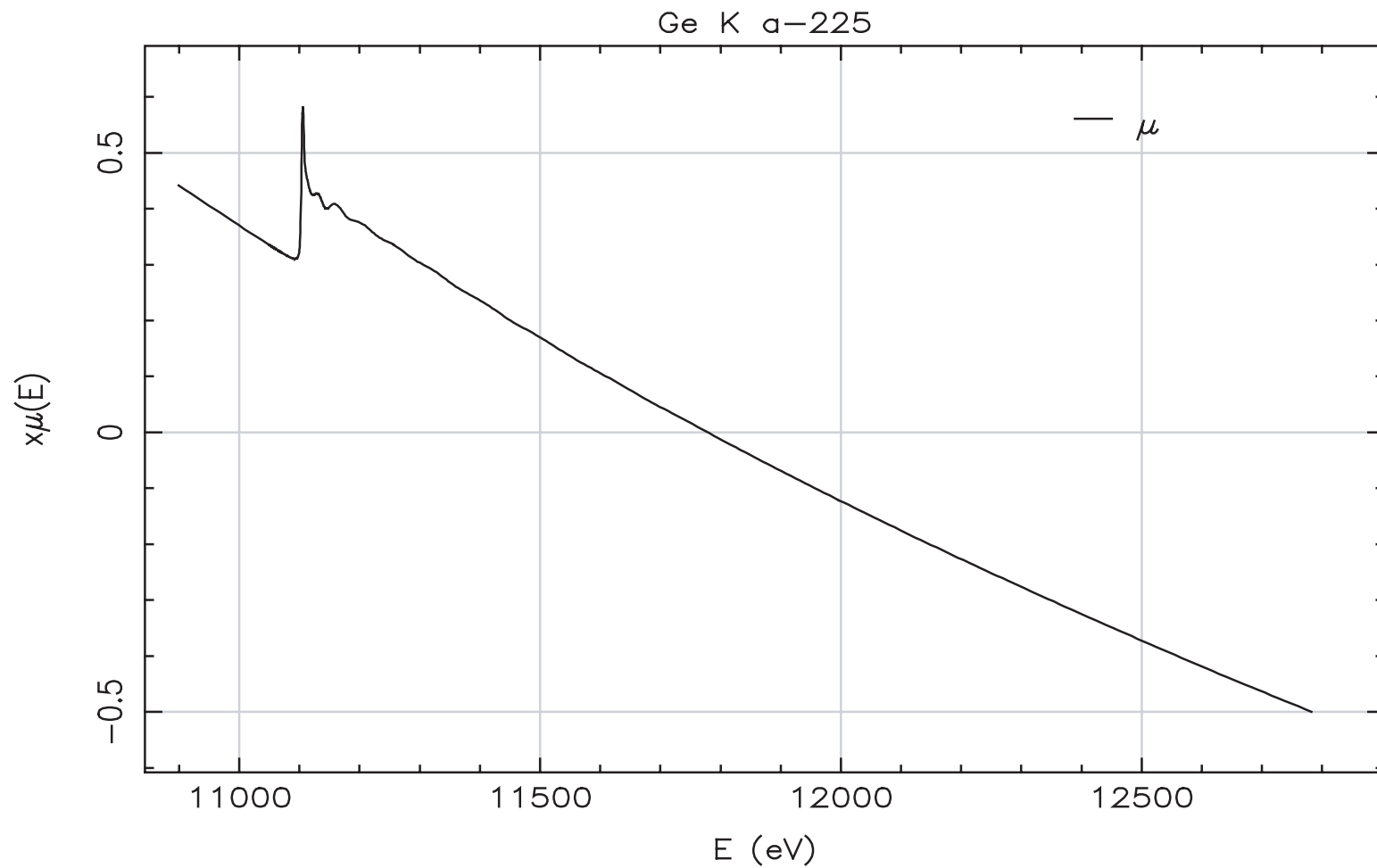


Figure 6.4 – Raw EXAFS spectrum of the Ge K-edge for the amorphous $\text{Ge}_2\text{Sb}_2\text{Te}_5$ sample.

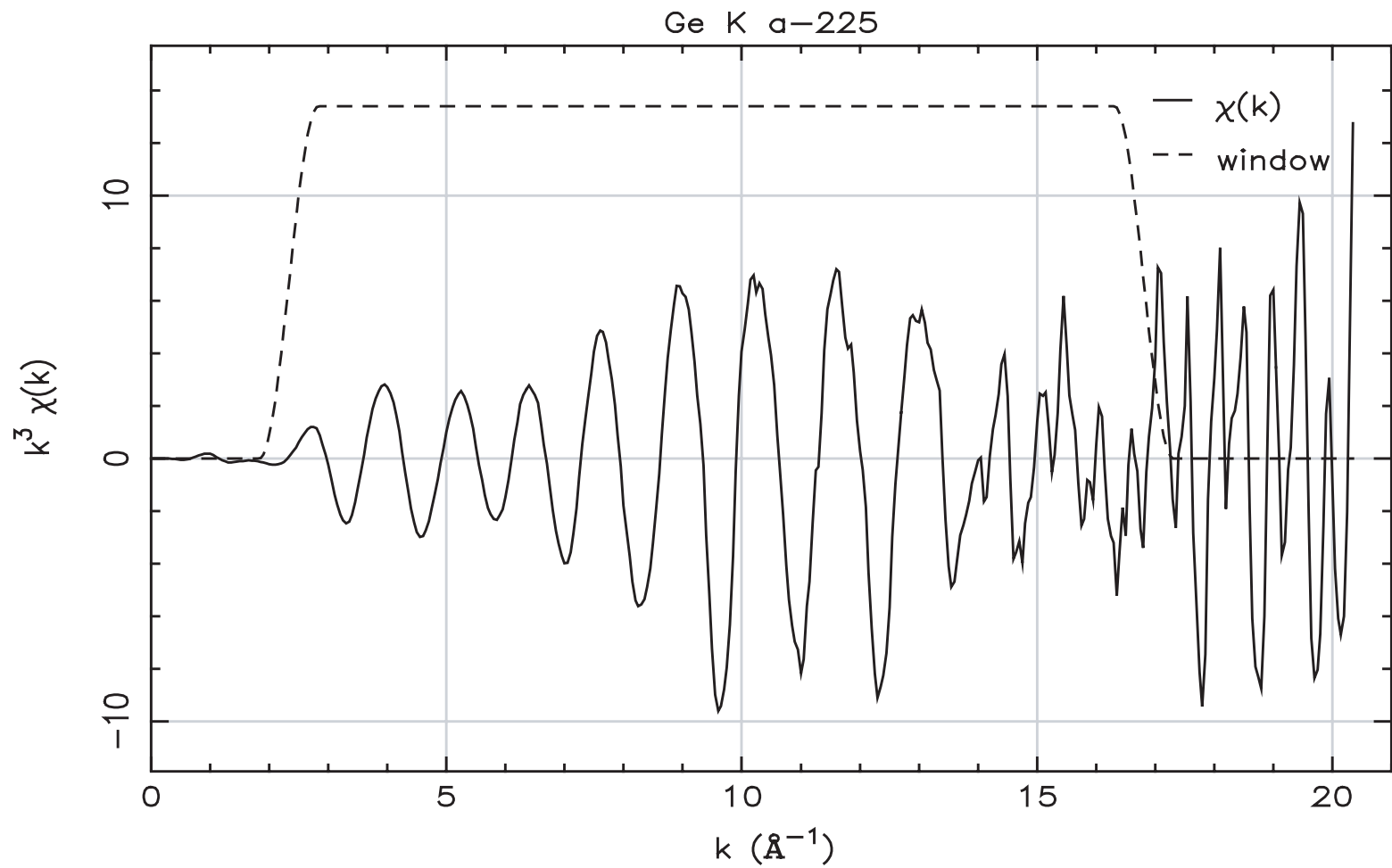


Figure 6.5 – $\chi(k)$ spectrum of the Ge K-edge for the amorphous $\text{Ge}_2\text{Sb}_2\text{Te}_5$ sample. The Fourier transform window is the dashed line.

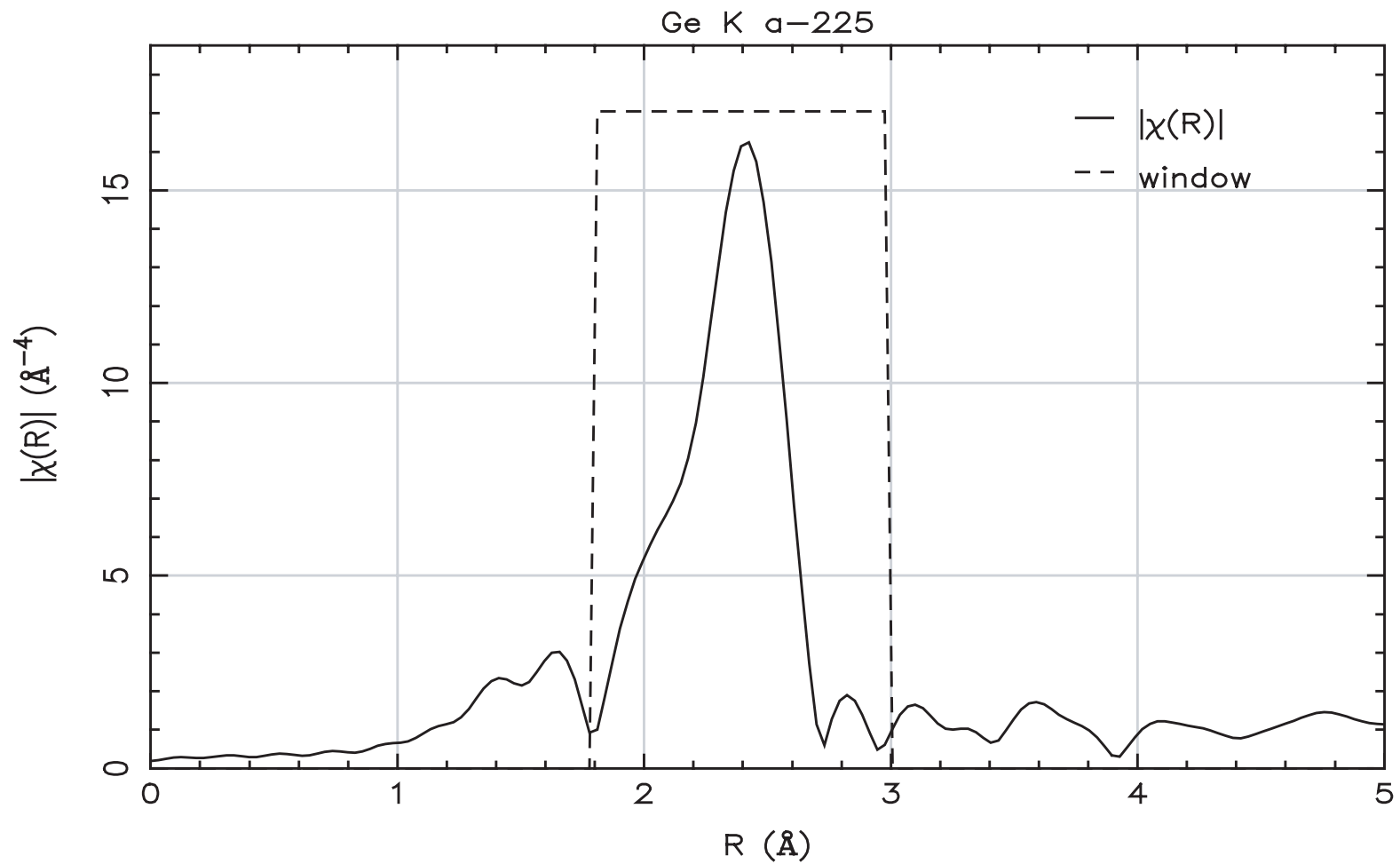


Figure 6.6 – $\chi(R)$ spectrum of the Ge K-edge for the amorphous $\text{Ge}_2\text{Sb}_2\text{Te}_5$ sample. The Fourier transform window is the dashed line.

6.5 References

- Bachrach, R. Z., Ed., Synchrotron Research, Springer, New York, (1992).
- Bethe, H., and Salpeter, E., in “Quantum Mechanics of One and Two Electron Systems”, Springer Verlag, Sec. 59 and 69, (1957).
- Bianconi, A., in: EXAFS and Near Edge Structure, eds. A. Bianconi, L. Incoccia and S. Stripcich, (Springer-Verleg, 1983)
- Boyce, J. B. and Hayes, T. M., in Physics of Superionic Conductors, ed. M. B. Salamon, Vol. 15, Ch. 2, Springer, New York, (1979)
- Crozier, E. D., in EXAFS Spectroscopy, edited by B. K. Teo and D. C. Joy, Plenum, New York (1981), pp.89.
- Crozier, E. D., and Seary, A. J., *Can. L. Phys.* **58**, 1388 (1980).
- Eisenberger, P., and Brown, G. S., *Solid State Comm.* **29**, 481 (1979).
- Filipponi, A., Di Cicco, A., and Natoli, C. R., *Phys. Rev. B* **52**, 15122 (1995)
- Fricke, H., *Phys. Rev.* **16**, 202 (1920)
- Friedrich, I, Weidenhof, V., Lenk, S., and Wuttig, M., *Thin Solid Films* **389**, 239-244 (2001)
- Godwin, R. P., *Springer Tracts Mo. Phys.* **51**, 1 (1968).
- Hayes, T.M. and Boyce, J. B. in *Solid State Physics*, Vol. 37 of Solid State Physics, edited by H. Ehrenreich, F. Seitz, and D. Turnbull, Academic Press, New York, (1982)
- Hertz, G., *Z. Phys.* **3**, 19 (1920)
- ID-10 website, Online at
- https://beam.aps.anl.gov/pls/apsweb/beamline_display_pkg.display_beamline?p_beamline_num_c=10

- Jackson, J. D., Classical Electrodynamics, Ch. 14, Wiley, New York, (1999).
- Karpinski, O. G., Shelimova, L. E., Kretova, M. A., and Fleurial, J.-P., *Journal of Alloys and Compounds* **268**, 112-117 (1998).
- Kincaid, B. M., and Eisenberger, P., *Phys. Rev. Lett.* **34**, 1361 (1975).
- Koch, E. E., Ed., in Handbook on Synchrotron Radiation Research, North Holland, New York, (1983).
- Kostarev, A. I., *Zh. Eksper. Teor. Fiz.* **11**, 60 (1941).
- Kronig, R. de L., *Z. Physik.* **70**, 317 (1931).
- Kronig, R. de L., *Z. Physik.* **75**, 468 (1932).
- Lee, P. A., and Beni, G., *Phys. Rev. B* **15**, 2862 (1977).
- Lee, P. A., and Pendry, J. B., *Phys. Rev. B* **11**, 2795 (1975).
- Margaritondo, G., Ed., in Introduction to Synchrotron Radiation, Oxford University Press, (1988).
- Martens, G., Rabe, P., Schwentner, N., and Werner, A., *Phys. Rev. Lett.* **39**, 1411 (1977).
- Nelson, W. F., Siegel, I., and Wagner, R. W., *Phys. Rev.* **127**, 2025 (1962).
- Newville, M., *J. Synchrotron Rad.* **8**, pp 322--324 (2001).
- Newville, M., Līviņš, P., Yacoby, Y., Rehr, J.J., and Stern, E.A., *Physical Review B* **47**, 14126 (1993).
- Peterson, H., *Z. f. Phys.* **98**, 569 (1936).
- Ravel, B. and Newville, M., *J. Synchrotron Rad.* **12**, pp 537--541 (2005).
- Rehr, J.J., and Albers, R.C., *Rev. Mod. Phys.* **72**, 621-654 (2000)
- Rehr, J. J., Davidson, E. R., Martin, R. L., and Stern, E. A., *Phys. Rev. B* **17**, 560 (1987)

Rehr, J.J., Mustre de Leon, J., Zabinsky, S.I., and Albers, T.C., J. Am. Chem. Soc. **113**, 5135 (1991).

Sawada, M., Rep. Sci. Works Osaka Univ. **7**, 1 (1959).

Sayers, D. E., and Bunker, B.A., Data Analysis. In “X-ray Absorption, Principles, Applications, Techniques of EXAFS, SEXAFS, and XANES”, E. by d. C. Koningsberger and R. Prins, ch. 6, (John Wiley and Sons, 1988)

Sayers, D. E., Lytle, F. W., and Stern, E. A., Adv. X-Ray Anal. **13**, 248 (1970).

Sayers, D. E., Stern, E. A., and Lytle, F. W., Phys. Rev. Lett. **27**, 1204 (1971).

Schift, L. I., in Quantum Mechanics, McGraw Hill Ltd., p 404 (1968).

Schmidt, V. V., Bull. Acad. Sci. Ussr, Ser. Phys. **25**, 998 (1961).

Schwinger, J., Phys. Rev. **75**, 1912 (1949).

Segre, C., Private Communication

Sokolov, A. A., and Ternov, I. M., Synchrotron Radiation, Pergammon Press, New York, (1968).

Stern, E. A., Phys. Rev. B **10**, 3027 (1974).

Stern, E. A., Heald, S.M., and Bunker, B., Phys. Rev. Lett. **42**, 1372 (1979)

Stern, E. A., and Rehr, J. J., Phys. Rev. B **27**, 3351 (1983)

Stöhr, J., NEXAFS Spectroscopy, Springer 1992

Teo, B. K., and Lee, P. A., J. Am. Chem. Soc. **101**, 2815 (1979).

Yamada, N. and Matsunaga, T., J. Appl. Phys. **88**, 12 (2000).

Yinug, C. F., J. International Commerce and Economics, 1 (July 2007).

Chapter 7 – Results and Discussion

7.1 Introduction

As the previous chapters indicate, EXAFS analyses of three alloys in the Ge-Sb-Te system comprise a small fraction of the full breadth of this study. This chapter serves as the lynchpin of the whole study, joining together a quantitative experimental result with a comprehensive theoretical analysis to explain a portion of a complicated ternary system. I begin with a detailed examination of the experimental results.

7.2 EXAFS Results

Data analysis for the three alloys – $\text{Ge}_2\text{Sb}_2\text{Te}_x$ where $x = 4,5,7$ - follows the formulary laid out in chapter 6. To recap: data preprocessing and iterative background removal were carried out using the Athena software package. The Fourier transform and subsequent iterative fitting process was carried out with the Artemis software package, which generated both graphical fits and numerical results. The progression from raw data to Fourier transformed data from the Ge edge of $\text{Ge}_2\text{Sb}_2\text{Te}_5$ appears in chapter 6 as the example of the type and quality of data used in this study. This chapter will focus instead on trends in the data, followed by analysis of the results of the fitting procedure.

Figure 7.1 depicts the Fourier transformed spectra from the Ge edge of all three alloys. Figure 7.2 shows a typical fit for the edge (the $\text{Ge}_2\text{Sb}_2\text{Te}_5$ alloy) in R-space, figure 7.3 the same fit in back-transformed momentum space. Figures 7.4-7.5 and 7.6-7.7 show the same plots for the Sb and Te edges, respectively. For each set of data, the fitting model consists of a small cluster model – usually 5 or 6 atoms. This model size avoids any bias in the results toward a crystalline interpretation. Also, the fit took into account every possible

scatterer-backscatterer pair, as well as myriad geometries – tetrahedral, octahedral, pyramidal, square-planar – so as not to skew the results toward any specific composition or geometry. As expected, differing geometries played little to no role in the fitting process, as EXAFS is largely insensitive to that parameter.

Evidence of the lack of a scattering pair was manifest in an unacceptably large (typically >1000) chi-squared error obtained between the FEFF modeled pairs and observed data. The goodness of the fit is evident in the agreement between the dashed line fit and the solid line data shown in the typical fit figures. Of the six possible atom pairs, only four pairs showed acceptable fits, with no evidence for Te-Te bonds or Ge-Sb bonds evident in any of the edges. The absence of the Ge-Sb bond was confirmed in both the Ge- and Sb- edge measurements. Data for all samples appear as Table 7.1.

The data of Table 7.1 reveal important trends as the atomic fraction of Te is varied in alloys with equal atomic fractions of Ge and Sb. While the Debye-Waller factor (σ) and the phase (φ) represent important parameters involved in fitting the data, the coordination number (N) and the bond distance (R) provide one with important bonding information that leads to a deeper understanding of the atomic structure of $\text{Ge}_2\text{Sb}_2\text{Te}_x$ alloys. Examination of the errors associated with the determination of N and R, however, causes one to question the value of modeling based principally on N values where the error can be as much as one third of the value of N itself. R determination, on the other hand, is quite accurate with uncertainties generally less than one percent. Previous work on $\text{Ge}_2\text{Sb}_2\text{Te}_5$ [Baker et al.] relied on modeling that necessitated use of both N and R data. To refine the analysis, we were led to the present study that involves a survey of several $\text{Ge}_2\text{Sb}_2\text{Te}_x$ alloys and includes

a closer focus on R data in modeling alloy structure. This focus might be viewed as an attempt to do “abscissa-physics” in turning one’s attention away from the less reliable measurements of ordinate – i.e. N – values. That is, by monitoring alloy trends as a function of composition, and by exploiting principally R data, we develop a model of atomic structure that helps us understand alloy properties.

One other aspect of EXAFS studies that presents challenges in studies of GeSbTe alloys is the proximity of Sb and Te on the periodic table. Because of this proximity, Te and Sb resemble each other as back-scatterers. One has to be very careful in modeling because the small difference between Sb and Te can sometimes not be distinguished. This problem represents yet another reason to perform a systematic study across a family of alloys and to avoid basing conclusions on distinguishing between these atoms.

7.3 Discussion

The ternary alloy diagram of figure 7.8 provides a framework for the present compositional study. In the figure, alloys of $\text{Ge}_2\text{Sb}_2\text{Te}_x$ lie on the intersections of dashed lines as shown. The line bisecting the Te vertex simply identifies the locus of alloys with equal atomic fractions of Ge and Sb. The locus of good glass formers Sb_2Te_3 , Ge_2Te_3 , and GeTe_2 are indicated on the diagram’s edges. Also identified is the composition GeTe , which is not a good glass-former. Note that $\text{Ge}_2\text{Sb}_2\text{Te}_7$ lies on the intersection of the Te vertex bisector and the so-called Sb_2Te_3 - GeTe_2 tie line. Also shown in the figure is the locus of $\text{Ge}_2\text{Sb}_2\text{Te}_6$, a material that was not studied. This alloy lies at the intersection of the Te vertex bisector and the Sb_2Te_3 - Ge_2Te_3 tie line. While $\text{Ge}_2\text{Sb}_2\text{Te}_5$ does indeed lie on an intersection as shown, neither of these lines represents a true tie line that terminates on good glass

formers. The alloy $\text{Ge}_2\text{Sb}_2\text{Te}_4$ does not lie on any intersection of interest. In some senses it is unfortunate that $\text{Ge}_2\text{Sb}_2\text{Te}_5$ lies at an intersection since one might be led to conclude that this alloy represents a pseudo-binary between the Sb_2Te_3 and GeTe end points. This is not the case, as the EXAFS data will show.

Consider $\text{Ge}_2\text{Sb}_2\text{Te}_7$. The Ge data indicate heteropolar four-fold coordinated Ge-Te bonds. That is, all Ge is bonded in GeTe_2 configurations with each Ge surrounded by four Te atoms. All Sb atoms are three-fold coordinated to Te neighbors in an Sb_2Te_3 configuration. The end points of the tie line on which $\text{Ge}_2\text{Sb}_2\text{Te}_7$ is located are the glass-formers GeTe_2 and Sb_2Te_3 . Thus, $\text{Ge}_2\text{Sb}_2\text{Te}_7$ is an amorphous pseudo-binary comprised of 2 parts GeTe_2 and one part Sb_2Te_3 with Te providing two-fold coordinated bonds linking these units.

Consider $\text{Ge}_2\text{Sb}_2\text{Te}_6$. While we did not measure this alloy, one might imagine that it would likewise be a pseudo-binary consisting of Sb_2Te_3 and Ge_2Te_3 units. This alloy lies on the tie line between these two good glass-formers. The fact that it is on the Te vertex bisector merely suggests equal amounts of Sb_2Te_3 and Ge_2Te_3 in $\text{Ge}_2\text{Sb}_2\text{Te}_6$. While this structure is speculation, analysis of $\text{Ge}_2\text{Sb}_2\text{Te}_5$ lends support to these conclusions.

Consider $\text{Ge}_2\text{Sb}_2\text{Te}_5$. The Ge data show that 6/39 (or 15%) of the Ge bonds are homopolar. The Ge_2Te_3 unit has seven bonds, one of which (or 14%) is homopolar. The EXAFS data thus suggest that in $\text{Ge}_2\text{Sb}_2\text{Te}_5$ all Ge is bonded in Ge_2Te_3 configurations. The antimony data show all Sb to be in pyramidal Sb_2Te_3 configurations again. The Te data suggest a possible over-coordination of 2.4, but the error bars on the N values are so large as to make such a conclusion questionable at best. The Sb data, on the other hand, indicate an

interesting feature for which considerable confidence in R values exists. A short Sb-Te bond at 2.50 Å is clearly evident. This distance is appreciably less than the covalent bond distance of 2.82 Å. There are two possible explanations for the existence of this short distance – both of which suggest the presence of Te_3^+ units. We discuss each in turn.

The positive charge carried by any Te_3^+ units present in an alloy would be distributed somewhat throughout the vicinity of the Te atom. This redistribution of excess positive charge is tantamount to a diminution of negative charge which would have the effect of shortening the covalent bonds of the Te to neighboring atoms. As shown in figure 7.9, the effect would be stronger for any neighboring Sb atom in particular since the Sb and Te bonding involves similar 4p electrons from each atom. The effect on Sb-Ge bonds would be less due to the different nature of the bonding (4p from the Sb and 5p from the Ge). If this configuration is responsible for the observed short Te-Sb bond, the observation is evidence of the presence of Te_3^+ configurations.

In an alternative explanation shown in figure 7.10, the shorter Te-Sb bond is understood as an electrostatic bond between a three fold coordinated Te, which is near to the non-bonded symmetric pyramidal axis of an Sb_2Te_3 configuration. Note that the Sb_2Te_3 unit has a pair of non-bonding electrons at this position, so this side of the Sb_2Te_3 unit has a relatively negative charge that attracts the positively charged Te_3^+ . Of course the full Sb_2Te_3 unit itself is neutral. If this explanation is correct, once again the presence of the short Sb-Te bond becomes corroborating R value evidence for over coordinated Te_3^+ . In either case, the R data confirms the suggestion of the less confident N data.

Consider $\text{Ge}_2\text{Sb}_2\text{Te}_4$. Again, the number of homopolar Ge bonds suggests that all Ge exists in Ge_2Te_3 configurations as with $\text{Ge}_2\text{Sb}_2\text{Te}_5$. The short Sb-Te bond is again in evidence, thus indicating the presence of Te_3^+ units. Indeed, the N data suggest that there may be more such units in $\text{Ge}_2\text{Sb}_2\text{Te}_4$ than in $\text{Ge}_2\text{Sb}_2\text{Te}_5$. In viewing these two alloys on the ternary diagram of figure 7.8 they may be considered to be systems that are comprised of Sb_2Te_3 and Ge_2Te_3 units with increasing amounts of Te_3^+ as one moves further from Te along the Te vertex bisector (that is from $\text{Ge}_2\text{Sb}_2\text{Te}_5$ to $\text{Ge}_2\text{Sb}_2\text{Te}_4$.) They are not, therefore, pseudo-binaries, but are instead chemically ordered ternary alloys.

7.4 Constraint Counting

Consider first the local bonding environment for Ge in a generic sense. The results in table 7.1 give a total coordination for Ge of approximately four in each alloy, an indication of tetrahedral coordination for all of the Ge atoms. To zeroth order, using Eq. (2), a tetrahedral Ge configuration yields $C_{av} = 7$, with five bending and two stretching constraints/atom. However, the combination of homopolar (Ge-Ge) and heteropolar (Ge-Te) bonds in $\text{Ge}_2\text{Sb}_2\text{Te}_4$ and $\text{Ge}_2\text{Sb}_2\text{Te}_5$ has a profound effect on constraint counting in those systems; bond-bending constraints can be removed by considering in detail the specific bonding configuration. In particular, bending constraints around each Ge atom are a mixture of Ge-Ge-Te and Te-Ge-Te motions. As noted in chapter 4, the force constant for the Ge-Ge-Te bending motion is significantly reduced with respect to that of a Te-Ge-Te bending motion due to the different Ge-Ge-Te and Te-Ge-Te bond energies. This permits the removal of 2.67 bending constraints (1.67 from two doubly-degenerate E-mode vibrations and 1 for a non-degenerate A-mode vibration) for the Ge_2Te_3 arrangement. Our results yield a bonding

model in which all of the Ge atoms are in this configuration, thus the total number of bond-bending constraints around the average Ge atom are reduced from 5 to 2.33. This in turn reduces the total number of constraints for Ge atoms from 7 to 4.33.

In the Sb bonding environment, a three-fold pyramidal structure, there are 1.5 stretching constraints and 3 bending constraints, resulting in 4.5 total constraints. None of these constraints are broken; therefore, one finds the total constraints around the Sb atoms to be 4.5.

Table 7.1 indicates overcoordination of Te, which is supported by the following bond-counting exercise. The proposed model gives GST as a combination of Ge_2Te_3 and Sb_2Te_3 structural units. This counting results in a deficiency in Te for the GST composition, as stoichiometry requires that the addition of these two units equal $\text{Ge}_2\text{Sb}_2\text{Te}_6$. This 1/6, or ~17%, Te deficiency is reflected in our results, as the percent of over-coordinated Te determined from these fits is $0.4/2.4 \approx 17\%$. A Te deficiency, combined with full coordination of Ge and Sb require that some Te atoms over-coordinate, resulting in the presence of both two-fold and three-fold geometries. No constraints can be removed for the former configuration, and in the latter, constraints are removed, but proportionally so [Kerner and Phillips], resulting in 2 constraints for both configurations.

For the samples measured here (and for the speculated structure of $\text{Ge}_2\text{Sb}_2\text{Te}_6$) we can then calculate the average number of constraints per atom C_{av} for all four alloys. In general the expression is

$$C_{av}(\text{Ge}_l\text{Sb}_m\text{Te}_n) = \frac{l(C_{\text{Ge}}) + m(C_{\text{Sb}}) + n(C_{\text{Te}})}{l + m + n}, \quad (7.1)$$

and for the four alloys considered here this becomes

$$C_{av}(Ge_2Sb_2Te_4) = \frac{2(4.33) + 2(4.5) + 4(2)}{8} = 3.21, \quad (7.2)$$

$$C_{av}(Ge_2Sb_2Te_5) = \frac{2(4.33) + 2(4.5) + 5(2)}{9} = 3.07, \quad (7.3)$$

$$C_{av}(Ge_2Sb_2Te_6) = \frac{2(4.33) + 2(4.5) + 6(2)}{10} = 2.97, \quad (7.4)$$

and

$$C_{av}(Ge_2Sb_2Te_7) = \frac{2(7) + 2(4.5) + 7(2)}{11} = 3.36. \quad (7.5)$$

The calculations of equations 7.2-7.5 show that $Ge_2Sb_2Te_4$ and $Ge_2Sb_2Te_7$ are stressed-rigid materials with $C_{av} > 3$ and that $Ge_2Sb_2Te_5$ and $Ge_2Sb_2Te_6$ are intermediate phase materials with $C_{av} \approx 3$. One might consider that either of the latter two would be a good candidate for use as a phase change alloy. The fact that $Ge_2Sb_2Te_5$ has found use as such an alloy and $Ge_2Sb_2Te_6$ has not could lie in the presence of Te_3^+ found in $Ge_2Sb_2Te_5$ and its absence in $Ge_2Sb_2Te_6$. If, as suggested above, the Te_3^+ units provide nucleation centers for crystallization, this would explain the alloys' behavior. The EXAFS data suggest that this is the case.

7.5 Conclusion

EXAFS studies of as deposited a- $Ge_2Sb_2Te_x$ ($x = 4, 5, \text{ and } 7$) alloys interpreted in light of bond constraint theory lead to conclusions about the nature of these and other alloys. In particular, $Ge_2Sb_2Te_5$ and $Ge_2Sb_2Te_6$ are intermediate phase materials while $Ge_2Sb_2Te_4$ and $Ge_2Sb_2Te_7$ are stressed-rigid. $Ge_2Sb_2Te_6$ is a pseudo binary of Sb_2Te_3 and Ge_2Te_3 while $Ge_2Sb_2Te_5$ is a chemically ordered ternary alloy comprised of Sb_2Te_3 and Ge_2Te_3 embedded in a network of connecting Te that includes a measurable fraction of tellurium atoms bonded

in Te_3^+ configurations. These unusual bonding configurations may provide nucleation centers that are crucial for repeatable phase change behavior.

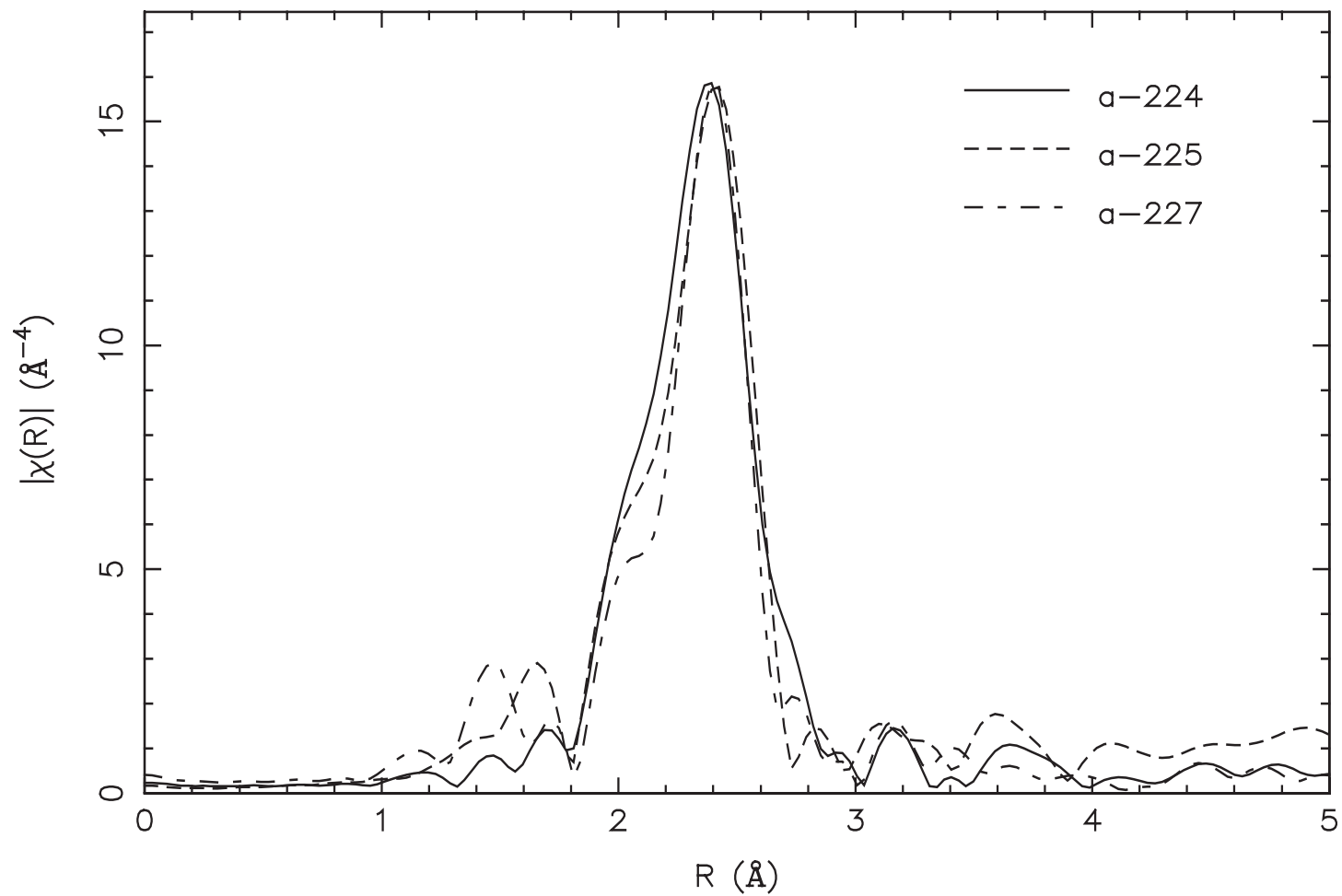


Figure 7.1 - $\chi(R)$ spectrum of the Ge K-edge for all three samples.

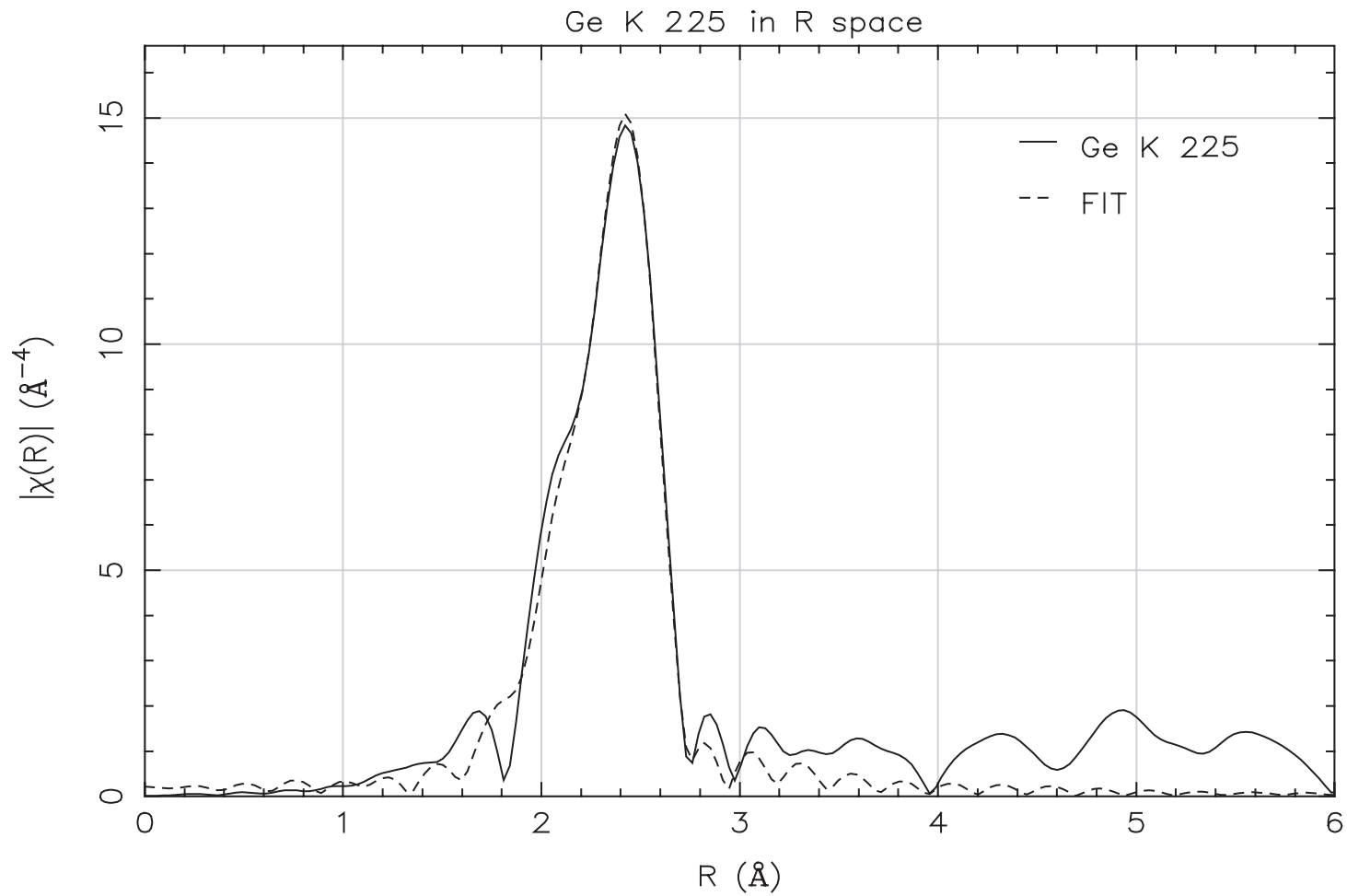


Figure 7.2 - $\chi(R)$ spectrum of the Ge K-edge for the amorphous $\text{Ge}_2\text{Sb}_2\text{Te}_5$ sample. The solid line is data, the dashed line is the fit.

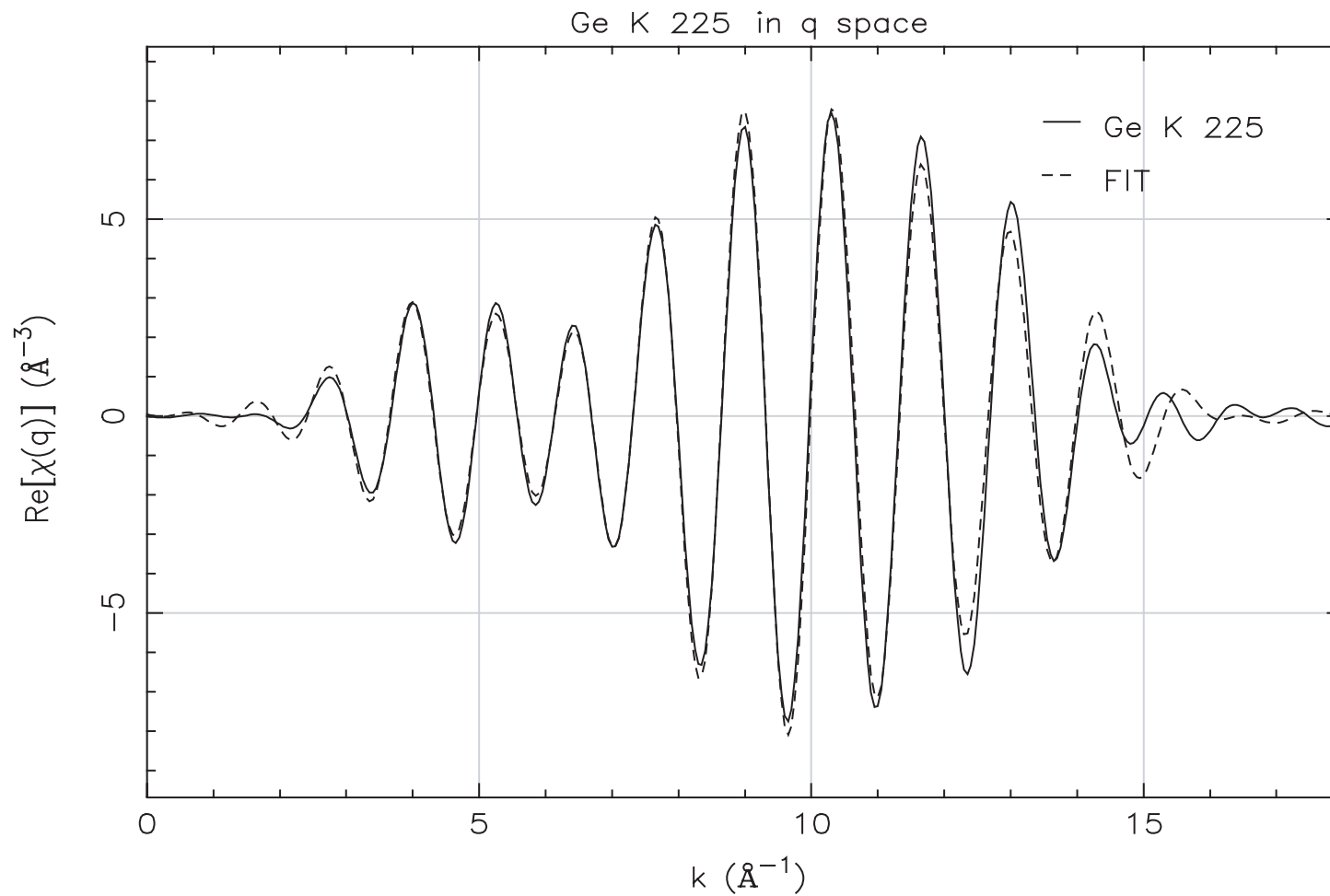


Figure 7.3 - $\chi(q)$ spectrum of the Ge K-edge for the amorphous $\text{Ge}_2\text{Sb}_2\text{Te}_5$ sample. The solid line is data, the dashed line is the fit.

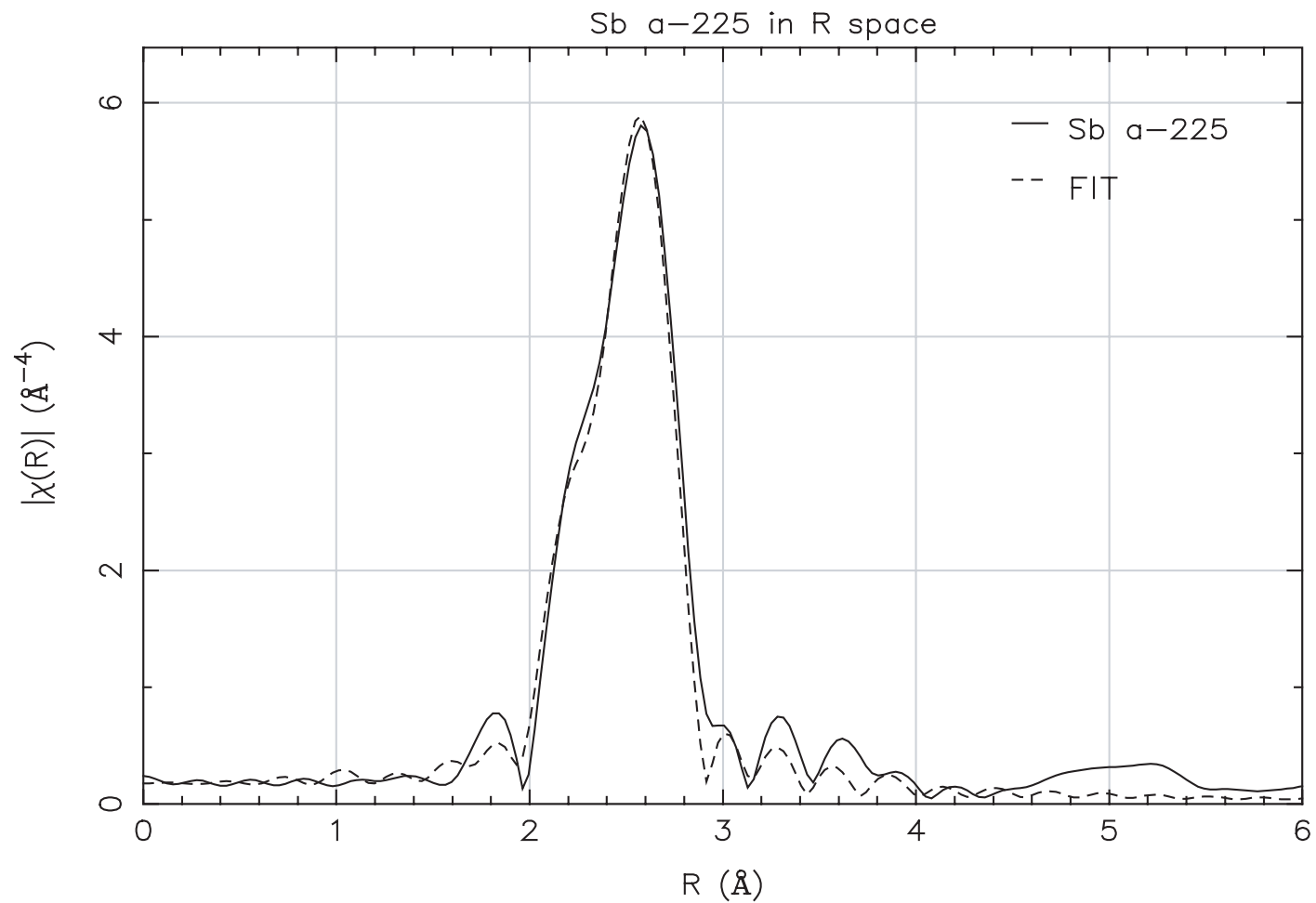


Figure 7.4 - $\chi(R)$ spectrum of the Sb K-edge for the amorphous $\text{Ge}_2\text{Sb}_2\text{Te}_5$ sample. The solid line is data, the dashed line is the fit.

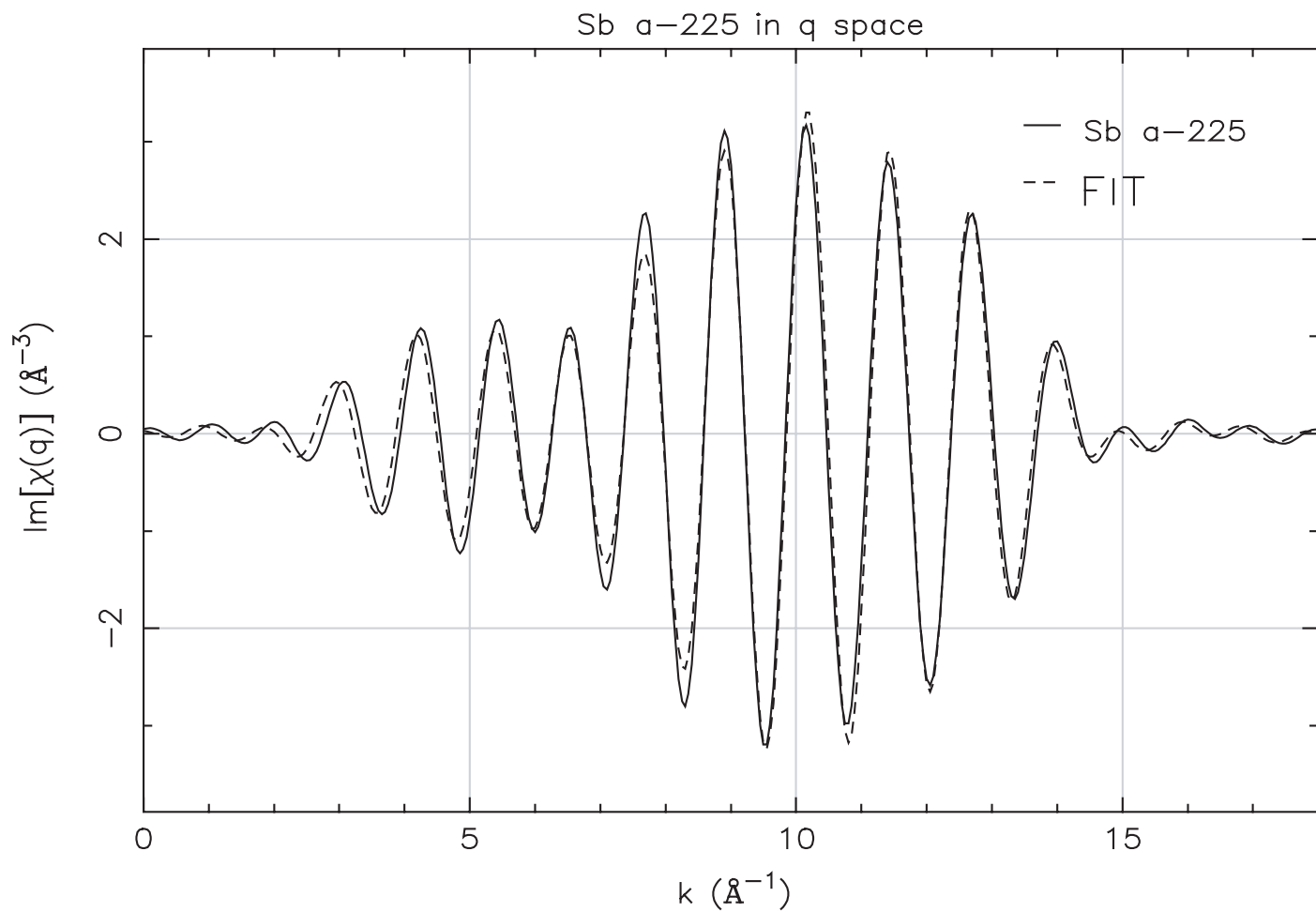


Figure 7.5 - $\chi(q)$ spectrum of the Sb K-edge for the amorphous $\text{Ge}_2\text{Sb}_2\text{Te}_5$ sample. The solid line is data, the dashed line is the fit.

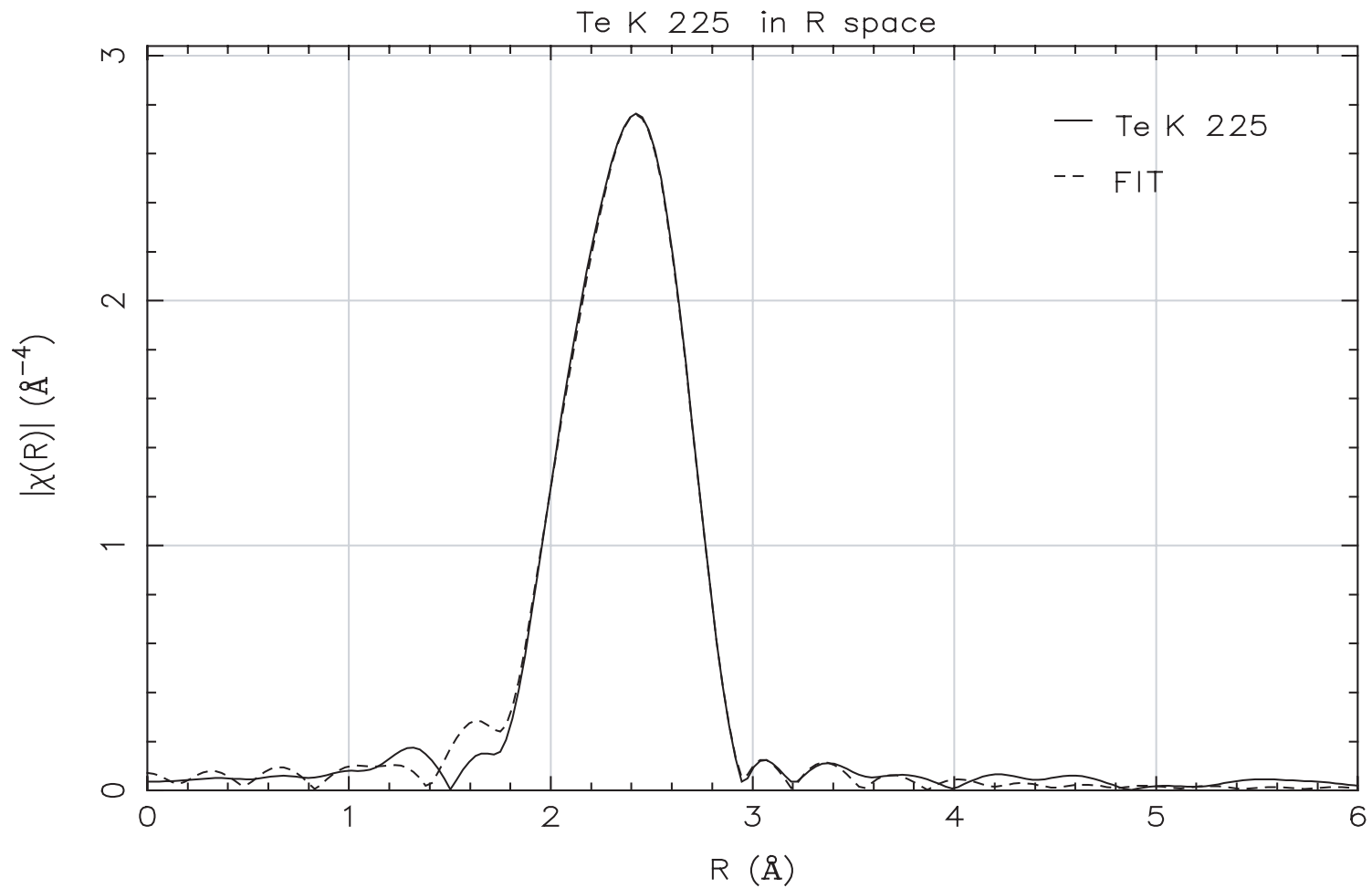


Figure 7.6 - $\chi(R)$ spectrum of the Te K-edge for the amorphous $\text{Ge}_2\text{Sb}_2\text{Te}_5$ sample. The solid line is data, the dashed line is the fit.

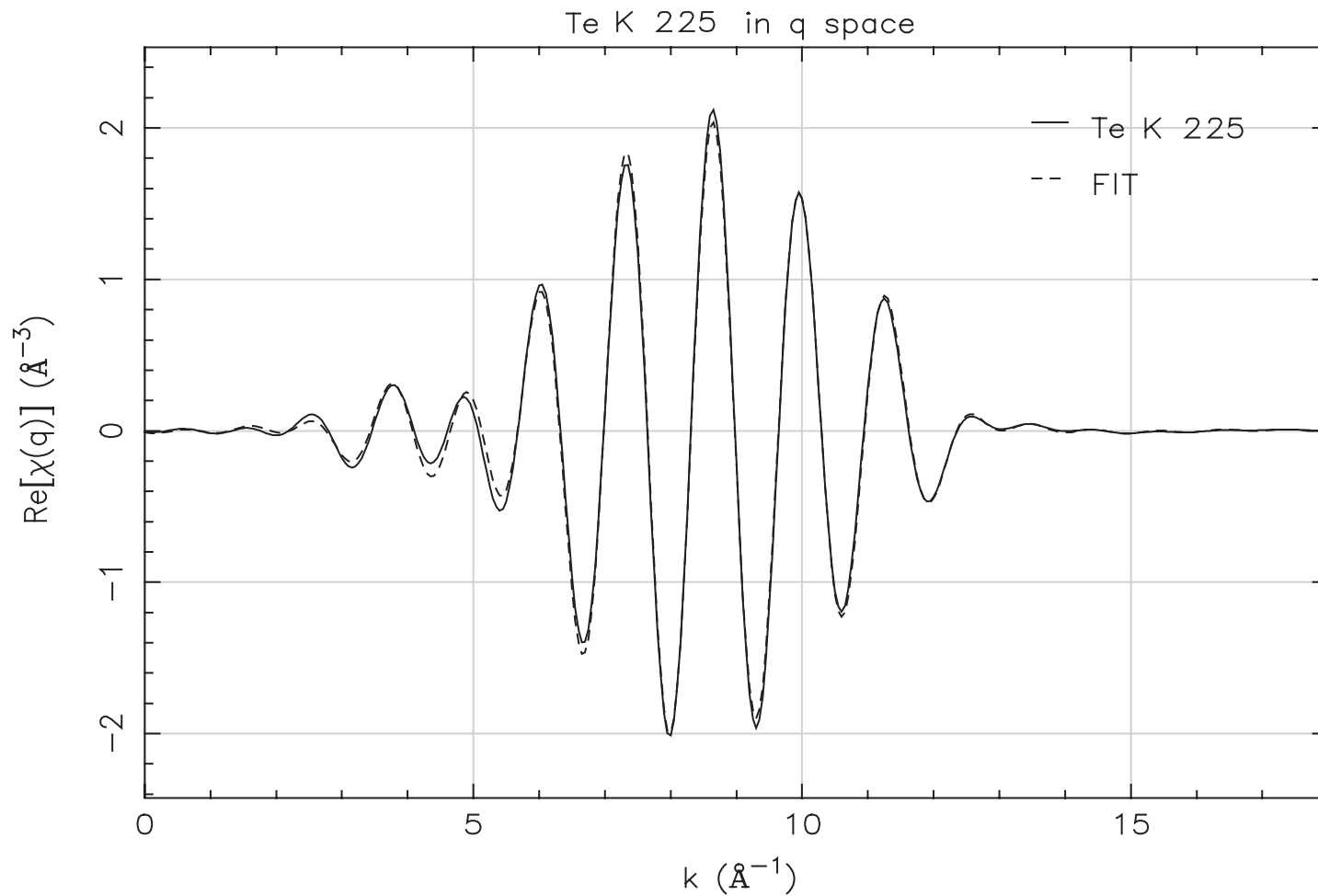


Figure 7.7 - $\chi(q)$ spectrum of the Te K-edge for the amorphous $\text{Ge}_2\text{Sb}_2\text{Te}_5$ sample. The solid line is data, the dashed line is the fit.

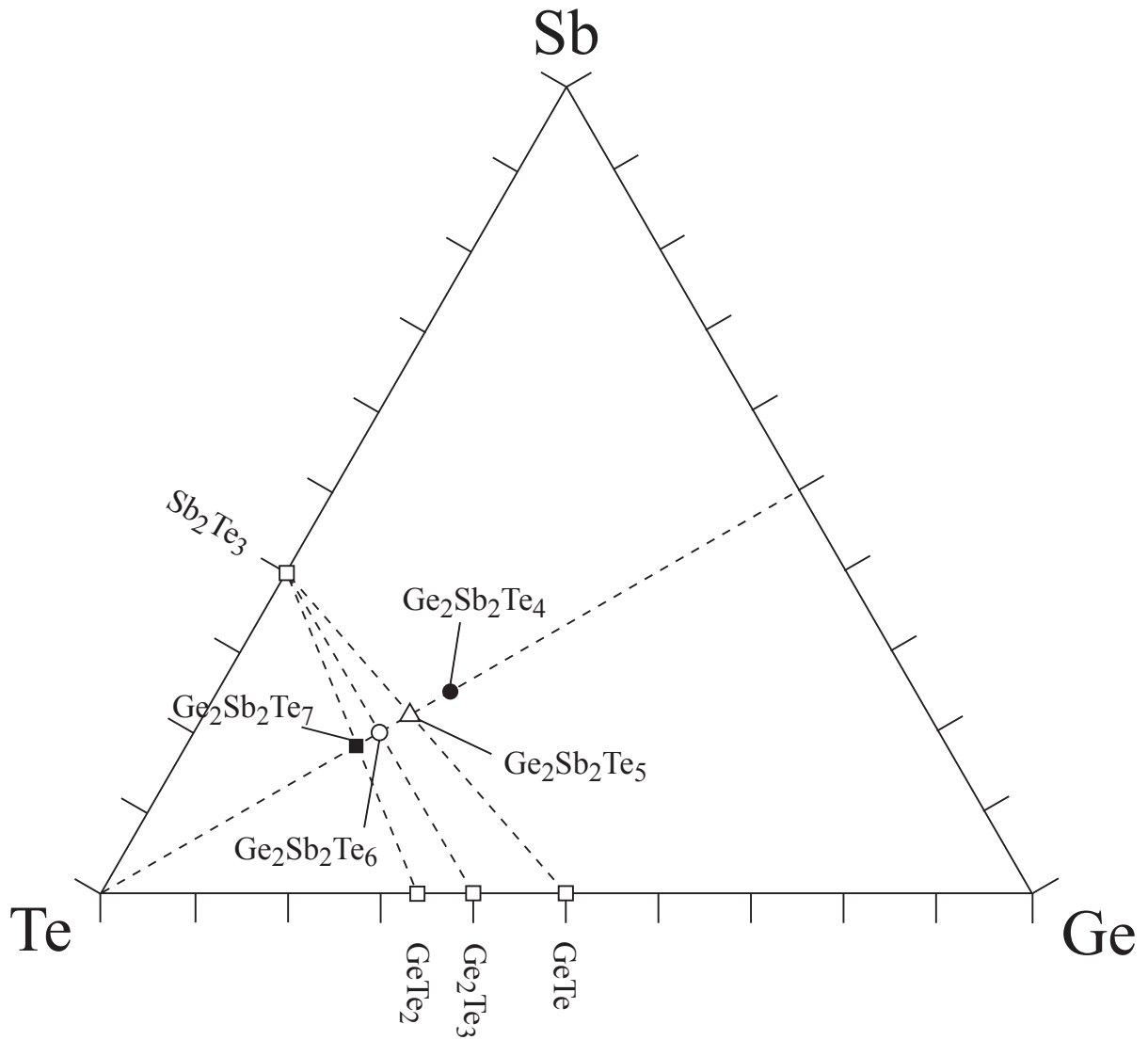


Figure 7.8 - $\chi(R)$ spectrum of the Ge K-edge for the amorphous $\text{Ge}_2\text{Sb}_2\text{Te}_5$ sample. The solid line is data, the dashed line is the fit.

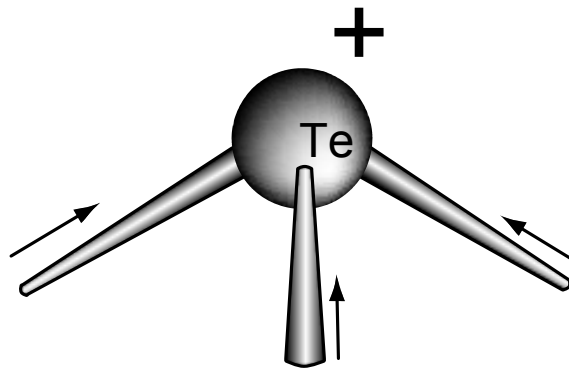


Figure 7.9 – Illustration of bond-shortening for overcoordinated Te atom.

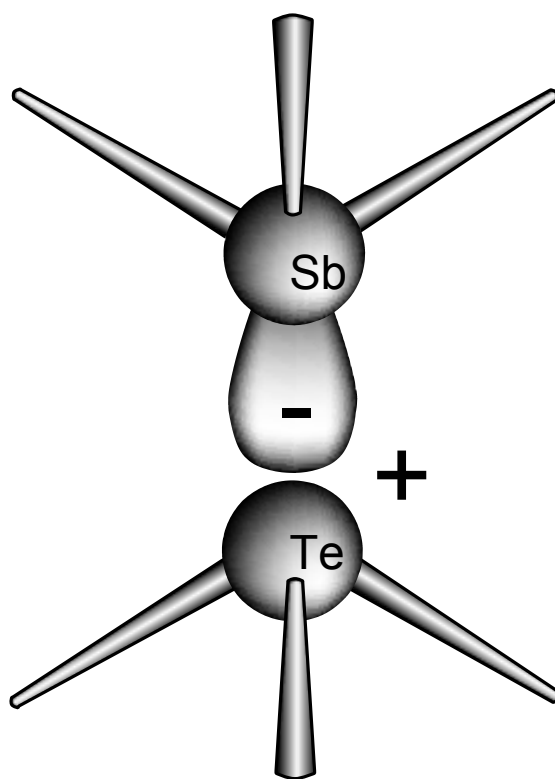


Figure 7.10 – Illustration of the Valence Alternation Pair (VAP) arising from overcoordinated Te atoms and resulting in a decreased Te-Sb distance as measured by EXAFS.

Table 7.1 – Coordination numbers (N), interatomic distances (R), phase shifts (E_0), and Debye-Waller factors (σ^2) for the $\text{Ge}_2\text{Sb}_2\text{Te}_x$ where $x=4, 5, 7$.

Alloy	Edge	Bond	N	R (Å)	E_0 (eV)	σ^2 (Å²)
a-224	Ge	Te	2.9 ± 0.4	2.63 ± 0.01	5 ± 2	0.007 ± 0.001
		Ge	0.8 ± 0.2	2.48 ± 0.01	6 ± 3	0.003 ± 0.001
	Sb	Te	3.0 ± 0.5	2.81 ± 0.02	5 ± 2	0.007 ± 0.002
		Te	1.2 ± 0.3	2.49 ± 0.02	7 ± 3	0.008 ± 0.002
	Te	Ge	1.1 ± 0.3	2.61 ± 0.01	7 ± 3	0.005 ± 0.002
		Sb	0.7 ± 0.2	2.83 ± 0.01	7 ± 2	0.005 ± 0.002
a-225	Ge	Te	3.3 ± 0.5	2.63 ± 0.01	6 ± 2	0.006 ± 0.002
		Ge	0.6 ± 0.2	2.47 ± 0.03	3 ± 1	0.003 ± 0.001
	Sb	Te	2.7 ± 0.4	2.82 ± 0.01	6 ± 2	0.005 ± 0.002
		Te	0.5 ± 0.2	2.50 ± 0.01	5 ± 2	0.008 ± 0.002
	Te	Ge	1.2 ± 0.3	2.62 ± 0.01	5 ± 1	0.006 ± 0.001
		Sb	1.2 ± 0.3	2.83 ± 0.01	4 ± 1	0.007 ± 0.002
a-227	Ge	Te	3.2 ± 0.8	2.60 ± 0.03	5 ± 1	0.006 ± 0.002
	Sb	Te	2.7 ± 0.4	2.82 ± 0.02	6 ± 1	0.006 ± 0.001
	Te	Ge	1.0 ± 0.2	2.60 ± 0.02	5 ± 1	0.005 ± 0.001
		Sb	1.0 ± 0.2	2.82 ± 0.02	5 ± 1	0.006 ± 0.002

2.5 References

Baker, D. A., Paesler, M. A., Lucovsky, G., Agarwal, S. C., and Taylor, P.C., Phys. Rev.

Lett. **96**, 255501 (2006).

Kerner, R., and Phillips, J. C., Solid State Communications, **117**, 47 (2001).